UC San Diego

UC San Diego Electronic Theses and Dissertations

Title

Development of a Room Temperature Microwave Impedance Microscope for Characterization of 2D Materials

Permalink

https://escholarship.org/uc/item/9j0110qf

Author

Cobb, Evan

Publication Date

2022

Peer reviewed|Thesis/dissertation

eScholarship.org Powered by the California Digital Library
University of California

UNIVERSITY OF CALIFORNIA SAN DIEGO

Development of a Room Temperature Microwave Impedance Microscope for Characterization of 2D Materials

A thesis submitted in partial satisfaction of the requirements
for the degree Master of Science

in

Physics

by

Evan Cobb

Committee in Charge:

Professor Monica Allen, Chair
Professor Richard Averitt
Professor Tenio Popmintchev

2022

The thesis of Evan Cobb is approved, and it is acceptable in quality and form for publication on microfilm and electronically.

University of California San Diego

2022

TABLE OF CONTENTS

Thesis Approval Page iii

Table of Contents iv

List of Figures vi

Acknowledgments ix

Abstract of the Thesis xi

1 Introduction 1

1.2 Theory of MIM 1

1.3 Applications and Prior Work 4

1.4 The MIM Circuit 4

1.4.2 Voltage Modulated MIM 6

2 Research and Results 7

2.2 Tabletop Atomic Force Microscope 7

2.2.2 MIM Probes 10

2.2.3 Modification for Chip Carriers 12

2.3 Impedance Matching Networks 13

2.3.1 λ/2 IMN Design 13

2.3.2 MHz IMN Design 16

2.4 1 GHz Circuit 17

2.4.1 Development 17

2.4.2 Initial Testing 18

2.5 MHz Circuit 24

2.5.1 Development 24

2.5.2 Initial Testing 25

2.5.3 Further Improvements 34

2.5.4 WTe_2 Tests 42

2.5.5 Graphene on $RuCl_3$ Tests 43

2.5.6 Nano3 Tests 45

2.6 2-10 GHz Circuit 47

2.6.1 Development 47

2.6.2 Initial Testing 48

3 Conclusion 50

Appendix A Circuit Diagrams..53

Appendix B Common Issues and Fixes 56

B.1 1 GHz MIM Circuit 56

B.2 MHz MIM Circuit 56

B.3 2-10 GHz MIM Circuit 58

Appendix C Notes on the Cryogenic Amplifier from my Visit to Cosmic Microwave Technology on 4/16/21..59

References 65

LIST OF FIGURES

Figure 1: Example MIM response curves at a) 100 MHz, b) 1 GHz, and c) 10 GHz. The transition region shifts to higher conductivities as the frequency increases. 3

Figure 2: Simplified diagram of MIM circuit adapted from [1]. 5

Figure 3: Photo of the tabletop AFM from Thorlabs 7

Figure 4: Large triangular gold markers for visual alignment of the AFM tip. Inset: Magnified view of the sample region showing smaller gold triangles for alignment via AFM imaging.........10

Figure 5: PrimeNano long probe (left) and RMN 25Pt300C probe (right). The PrimeNano probe's small octagonal bond pad the left side is linked by a buried metallic path, faintly visible in the image. 11

Figure 6: The LCC socket mounted on plastic pieces for height and held in place by screws....12

Figure 7: Diagram of λ/2 IMN (top) and example image (bottom) 14

Figure 8: Example frequency sweep obtained with the 2-10 GHz circuit using a λ/2 IMN. Note the quality of the match at each harmonic varies..15

Figure 9: The MHz IMN diagram (top) and picture (bottom). 17

Figure 10: Image of the 1 GHz MIM circuit 18

Figure 11: RF power to DC voltage relation for the power monitor in the 1GHz circuit (from minicircuits.com) 19

Figure 12: Example frequency sweep using the 1 GHz circuit to identify the matching resonance of a λ/2 IMN 19

Figure 13: RMN probe with a large gold bond pad 21

Figure 14: Top: AFM image of a graphite flake (left side) on bare SiO2 (right side). Bottom: MIM data recorded as the sample was scanned horizontally. The CH 1 and CH 2 data show repetitions that correlated with the motion of the stage, not the material the tip was in contact with. All three signals are relatively noisy. 23

Figure 15: Image of the MHz MIM circuit...25

Figure 16: Early MIM scans of graphite. a) Optical image of the graphite flake. b) MIM data taken as a function of time and wrapped to generate a 2D color plot. c) MIM data recorded after modifying the scanning software to send commands to the X- and Y-piezos. 27

Figure 17: (a) Optical, (b) AFM, and (c) MIM-Im images of aluminum squares on SiO2............28

Figure 18: MIM images of gold rectangles. a) Wide area scan. Inset: AFM image of gold rectangles. b) Small area scan showing warping from piezo hysteresis. 30

Figure 19: Encapsulated twisted bilayer graphene. a) Optical image. b) AFM image. c) Raw MIM image. d) MIM image after editing in Gwyddion to improve the contrast. 31

Figure 20: Consecutive MIM images showing gradual destruction of an exposed graphene flake (white) and nearby gold alignment marks (yellow) on an SiO2 substrate (red) 33

Figure 21: EDU-AFM1 software showing the grid representing the photosensor. The center of the laser is shown by the white circle with (X, Y) coordinates (XDIFF, YDIFF). The value of XDIFF before the tip makes contacts determines the relative force applied. 37

Figure 22: a) Wide area scan of a graphene flake with a small contact force. The blue rectangle marks the region covered by the small area scans. b) First small area scan, second scan overall. c) Fifth small area scan, sixth scan in total. 39

Figure 23: Bruker's AFM (left) and SCM (right) images of their SRAM sample [6]. 40

Figure 24: a) MIM-Re, b) MIM-Im, c) dC/dV-Amp, and d) dC/dV-Phase of the static random access memory sample from Bruker. The dC/dV-Amp signal (c) is largest in regions with minimal doping, while the dC/dV-Phase signal (d) helps distinguish between lightly n-doped regions (more purple) and lightly p-doped regions (more red). 41

Figure 25: WTe_2 sample. a) Optical image taken before transport or AFM/MIM scanning. b) Optical image taken after transport and AFM/MIM scanning. The Pd contacts connecting the large gold electrodes to the sample are damaged and a small tear in the sample is visible in the red circle. c) AFM image taken after AFM/MIM scanning… 43

Figure 26: $RuCl_3$ sample. a) Optical image taken before AFM/MIM scanning. b) Optical image taken after AFM/MIM scanning with the area scanned in (c) outlined by a red rectangle. c) MIM scan of the sample showing the second graphene flake in orange. The graphene flake is fractured into several sections and the region… 44

Figure 27: Data from the first tests using the MHz circuit in Nano3. a) AFM image of the SRAM sample. b) MIM-Ch1 image of the SRAM sample. c) dC/dV-Amp image of the SRAM sample. d) dC/dV-Phase image of the SRAM sample. e) MIM-Ch2 image of the encapsulated graphene sample. 46

Figure 28: Image of the 2-10 GHz MIM circuit 48

Figure 29: MIM-Im image of the Al squares recorded using the 2-10 GHz box..........................49

Figure 30: Spatial maps of the MIM-Re signal on a black-As sample simulated by COMSOL at a) 150 MHz, b) 3 GHz, and d) 10 GHz. Lateral scale is in μm. 52

Figure A.1: Circuit components inside the 1 GHz MIM box 53

Figure A.2: Circuit components outside the 1 GHz MIM box 53

Figure A.3: Circuit components inside the MHz box 54

Figure A.4: Circuit components outside the MHz box, including the bias tee for dC/dV measurements 54

Figure A.5: Circuit components inside the 2-10 GHz box 55

Figure A.6: Circuit components outside the 2-10 GHz box 55

Figure C.1: Left: Their 12K plate. The components here are mechanically and thermally anchored with copper foil, held in place with washers and screws with a layer of indium foil for improved thermal contact. You can see the threads in the plate are stainless steel, press-in washers. Right: Another picture of their 12K plate... …………………………………………….... 64

Figure C.2: Left: Picture of the packaging of the copper foil they use. Top: A homemade thermal strap soldered at one end and crimped to a ring terminal at the other. The twisted copper threads are from old speaker wire. Bottom: Close up of the crimping ring terminal they use… 64

ACKNOWLEDGEMENTS

I would like to acknowledge Randall Clark and visiting undergraduate Armando Guerrero who constructed the 1 GHz MIM circuit before I joined the project. Hanyi Lu and Alexander Cauchon performed early troubleshooting of the 1 GHz circuit and wrote the original MATLAB code for control of the digital attenuators. Leonard Cao assisted with troubleshooting at various stages through the last few years. Shreyas Shukla helped with in-depth troubleshooting of the 1 GHz circuit and, together with Qixuan Zhang, worked on alternative methods of controlling the Thorlabs AFM before Dr. Rajarshi Bhattacharyya developed the early versions of the MATLAB programs we use today. Raj and I worked closely on the MHz circuit and together we obtained the first MIM images in our group. Rajarshi completed the tests of the 2-10 GHz circuit (presented in section 2.6.2) independently while I was away for winter break. Chen Wu constructed the MHz circuit that yielded our first successful MIM images, performed the tests on WTe_2 (section 2.5.4), and assisted with the tests in Nano3 (section 2.5.6). Raj, Leonard, Qixuan, and Chen have been responsible for fabricating most of the non-commercial samples presented here, and many, many more that were used along the way. Visiting undergraduate Brittany Jiang helped develop several of the flake exfoliation procedures that are still in use today. Additionally, much of the work presented here would not have been possible without use of the Nano3 user facility at UCSD and the support of their excellent staff.

On a more personal level I would like to thank Raj, Leonard, Qixuan, and Chen for countless discussions about our projects, physics, and life in general. I have learned much from them about being a student, scientist, and friend.

I would also like to thank Professor Monica Allen, who took a risk on me in my second month at UCSD and invited me to help build her lab from the ground up. Her guidance brought me to where I am today, and I have learned more than I can say from my time working with her.

I am also grateful for the opportunities afforded me through the QISE-NET program. My involvement in QISE-NET would not have been possible without Monica’s support and that of

Dr. Filip Ronning, the third member of my QISE-NET triplet and a gracious host during my week-long visit to Los Alamos National Lab.

Thanks also to other supportive members of the physics department. Lester Brooks and Dirk Johnson have provided essential knowledge and support in setting up the new lab and are responsible for delivering a nearly infinite stream of packages to our lab door. Sharmila Poddar has helped me navigate many difficult decisions throughout my degree by sharing invaluable experience and a willing ear. Thanks also to Professors Richard Averitt and Tenio Popmintchev, for serving on my thesis committee along with Monica.

Finally, I would like to thank my Mom, my Dad, Derek, Ellis, Tristan, and Joy for listening to my frustrations and successes alike and supporting me the whole time. Michelle, I would not have made it this far without you and I look forward to seeing where we go next. And thank you also to the friends and family in my life who have supported me on this journey. Nathan, Becca, Ron, Lynn, Lee, Owen, Eli, Shelley, Neil, Jason, Susan, Patti, Wilbur, Emily, Jake, Zuben, Natalie, Randall, Robert, Ben, Cory, Katie, Shawn, Sarah, Rachel, Aidan, Anne, Justin, Erin, Daniel, Isaac, and Lauren, I am grateful.

Chapter 2 is coauthored with Allen, Monica. The thesis author was the primary author of this chapter.

ABSTRACT OF THE THESIS

Development of a Room Temperature Microwave Impedance Microscope for Characterization of 2D Materials

by

Evan Cobb

Master of Science in Physics

University of California San Diego, 2022

Professor Monica Allen, Chair

This thesis describes my efforts to construct and improve a room temperature microwave impedance microscope (MIM) for characterization of 2D materials. Three separate MIM circuits were built for operation in different frequency ranges and alternately integrated with a tabletop atomic force microscope. The 1 GHz circuit did not yield reasonable MIM data despite concentrated troubleshooting, but the MHz and 2-10 GHz circuits were validated and improvements to the hardware and scanning software reduced signal noise and increased system reliability. Metallic thin films, exfoliated van der Waals materials, and doped semiconductor samples were imaged to demonstrate spatial mapping of conductivity and dopant concentration.

1 Introduction

In this thesis I will present progress on constructing, testing, and improving our room temperature microwave impedance microscopy (MIM) system. MIM at its most basic can be thought of as a measurement of the capacitance between a sharp tip and a sample. The high frequency nature of the measurement requires a microwave circuit for generating, conditioning, and reading the signals. Achieving high spatial resolution requires a scanning probe microscope. A complete MIM system consists of an integration of these two components and its final performance will depend on the capabilities of both systems. This introductory section will focus primarily on explaining the operating principles of the microwave circuit with little attention to the SPM side of the system, which is essentially interchangeable.

1.2 Theory of MIM

An explanation of the MIM technique is given here, following Chapter 15 of Capacitance Spectroscopy of Semiconductors [1]. Simply speaking, an MIM circuit sends a microwave signal through an impedance matching network (IMN) to a sharp tip, and then demodulates the reflected signal into orthogonal components corresponding to the real and imaginary parts of the complex impedance of the tip-sample interface. The tip, usually with a diameter of 20-100 nm, is very small compared to the microwave's wavelength, so the tip-sample interaction is quasi-electrostatic, and MIM is considered a near-field technique. The quasi-electrostatic nature also allows us to describe the interaction in terms of the lumped elements Z_{ts} / Y_{ts} (tip-sample impedance / admittance) and Z_{probe} / Y_{probe} (probe impedance / admittance). The admittance of the probe, Y_{probe}, is effectively in parallel with Y_{ts}, and does not change significantly during a scan. The IMN transforms the total admittance ($Y_{total} = Y_{ts} + Y_{probe}$) into a new value $y(Y_{total})$,

which is close to the 1/50 Ω admittance of the coaxial cables and RF electronics (Y_0). The reflected signal from the IMN is given by

$$\Gamma = \frac{Y_0 - y(Y_{total})}{Y_0 + y(Y_{total})}$$

The measured MIM signal is just the original microwave signal, $V_{in}e^{i\phi}$, multiplied by the reflection coefficient Γ, which can be redefined in terms of a function $f(Y_{total})$.

$$MIM = V_{in}e^{i\phi}\Gamma(Y_{total}) = e^{i\phi}f(Y_{total})$$

The tip-sample admittance is much smaller than the probe admittance ($Y_{ts} \ll Y_{probe}$) so treating Y_{ts} as a small perturbation and expanding around Y_{probe} gives,

$$MIM \approx e^{i\phi}f(Y_{probe}) + e^{i\phi}f'(Y_{probe})Y_{ts}$$

Choosing ϕ such that the coefficient of Y_{ts} is real we can rewrite the MIM signal in terms of the complex tip-sample admittance and respectively real and complex constants r and c.

$$MIM \approx rY_{ts} + c$$

We can then separate the real and imaginary parts of the MIM signal and consider only the change in signal between two locations rather than the absolute signal.

$$\Delta MIM_{real} \approx rRe(\Delta Y_{ts})$$

$$\Delta MIM_{imag} \approx rIm(\Delta Y_{ts})$$

Changes in the MIM signal are much easier to interpret than the actual value of the measured signal at a given tip location, so this final step is not unjustified. MIM is typically used as a qualitative technique but extracting physical quantities from an MIM image is possible and easiest to do by comparing the relative MIM signal on the sample region in question to a sample region with known properties [2].

Careful simulations of a tip-sample geometry in COMSOL Multiphysics show how the MIM response changes as a function of conductivity and frequency. Highly insulating samples show little response in both the real and imaginary channels whereas highly conducting samples show little response in the real channel and a large response in the imaginary channel. In the middle of the range the real response reaches a maximum and the imaginary response smoothly transitions between the two extremes. The middle transition region shifts with the MIM frequency, so higher frequencies are more useful in probing more conductive samples.

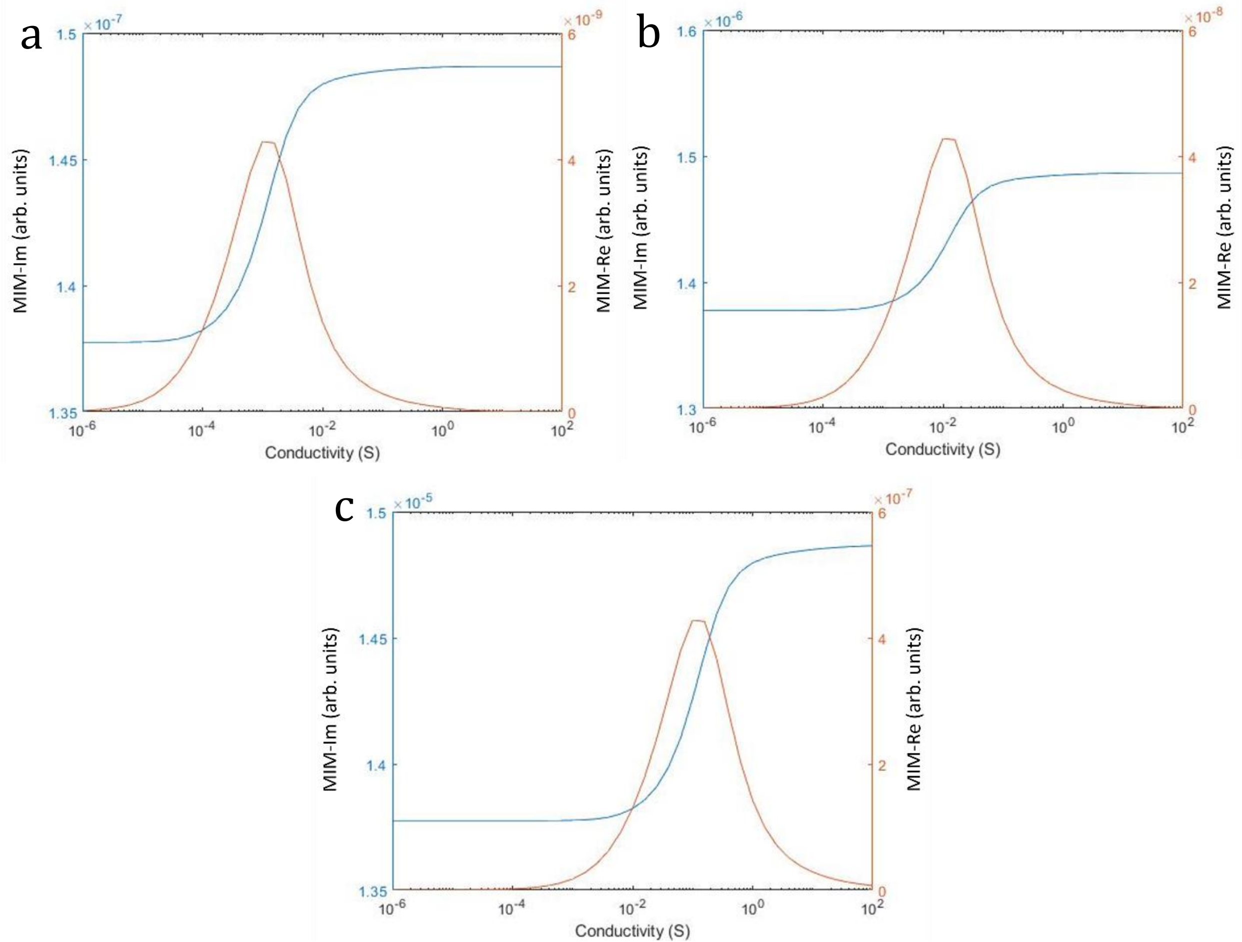

Figure 1: Example MIM response curves at a) 100 MHz, b) 1 GHz, and c) 10 GHz. The transition region shifts to higher conductivities as the frequency increases.

1.3 Applications and Prior Work

The MIM technique is applicable to many classes of classical and quantum materials, with recent work in the field focusing on strongly correlated electron systems and topological insulators [3]. The usefulness of MIM for understanding phase transitions and phase separations in complex oxides was demonstrated in a strained $Nd_{1/2}Sr_{1/2}MnO_3$ thin film grown on (110) $SrTiO_3$ [4]. MIM has also been used to explore emerging conductivity at order-parameter domain walls in materials like $Nd_2Ir_2O_7$ [5] and $Pr(Sr_{0.1}Ca_{0.9})_2Mn_2O_7$ [6]. In van der Waals heterostructures, MIM has been used to map local conductivity as a function of carrier density, and as a means of mapping electrical inhomogeneities [7], [8]. In the integer quantum Hall effect in graphene there is often a mismatch in the critical carrier density as measured by charge transport and capacitance spectroscopy, which was elucidated by MIM measurements that showed an unexpected increase of the gate-tuned carrier density near the flake edge [9]. MIM's ability to image buried conducting features proved useful in observing the quantum spin Hall effect in CdTe/HgTe quantum wells [10] and monolayer WTe2 [11] with protective capping layers. And an MIM study of the anomalous Hall effect in a $(Bi,Sb)_2Te_3$ film with thin Cr-rich layers on the top and bottom surfaces showed an unusual insulating state as an increasing magnetic field flipped the magnetization of the top and bottom layers [12]. These are just a few examples demonstrating the variety of applications of the technique. While this thesis is focused on the development of our room temperature MIM setup which has a relatively limited scope of application, the progress presented here has laid the groundwork for our cryogenic system and future additions to the body of knowledge outlined above.

1.4 The MIM Circuit

This section walks through the general structure of an MIM circuit (Figure 2). Our system-specific modifications to this general circuit design will be left out (e.g., our MHz circuit

combines the signal generator, reference line, and mixer in a single RF lock-in amplifier).

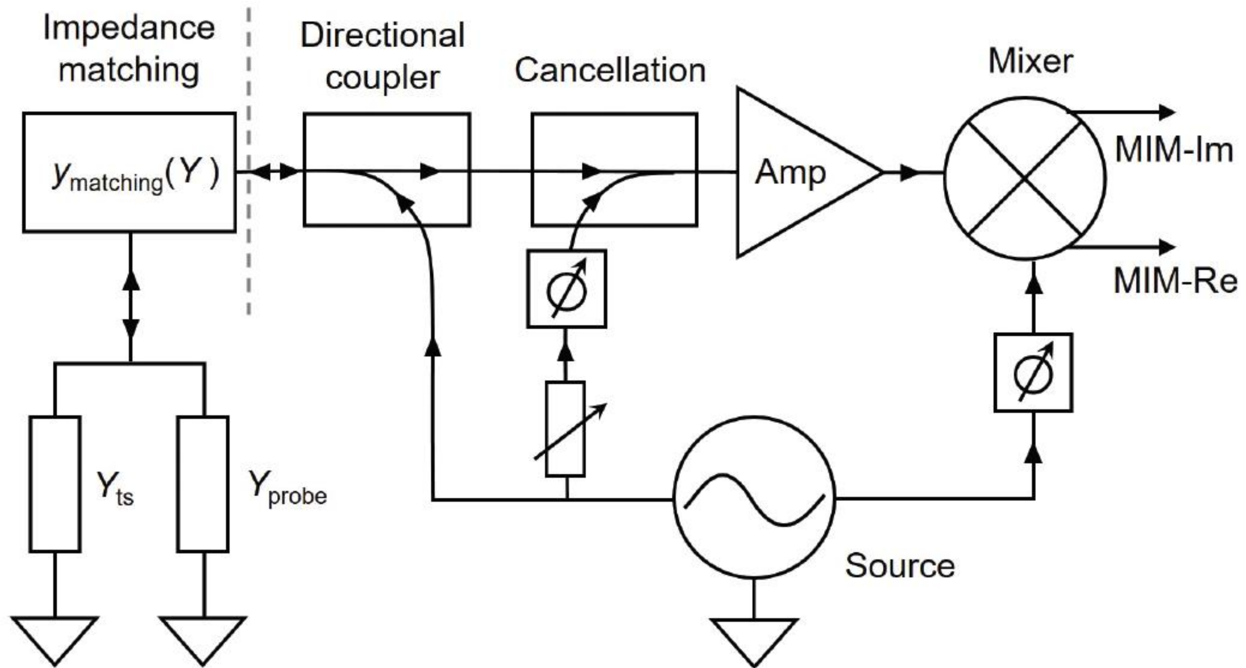

Figure 2: Simplified diagram of MIM circuit adapted from [1].

The signal generator outputs a microwave signal which is split by a power divider into a Reference signal and a Measurement signal. The Measurement signal goes to a second power divider and is split into the To Tip and Cancel signals. The To Tip signal is sent directly to the coupled port of a directional coupler, we'll call it directional coupler 1, and goes out of the input port to the impedance matching network. The To Tip signal continues to the probe where some of it is reflected from the sample surface and becomes the From Tip signal. The From Tip signal returns through the IMN to directional coupler 1 and straight through to directional coupler 2. Here it meets up with the Cancel signal which, after the power splitter, is passed through a variable phase shifter and attenuator before entering directional coupler 2 from the coupled port. The From Tip and Cancel signals typically pass through an amplifier and then on to the RF port of an IQ mixer. The Reference signal travels from the first power divider, through a phase shifter, and then to the LO port of the IQ mixer. The IQ mixer then uses the signal it receives from the LO port to essentially lock-in to the correct frequency and phase and split the signal it

receives in the RF port into in-phase and quadrature (out-of-phase) components. When the phase of the Reference signal is properly tuned, the in-phase and out-of-phase components correspond to the real and imaginary components of the complex impedance.

Due to imperfect impedance matching at the IMN, the static impedance of the probe (Y_{probe} from section 1.2), and imperfect connections within the circuit, it is expected that the tip-sample impedance which is the object of the measurement is drowned out by “junk” reflections. The Cancel line is used to negate this noise by creating a signal equal in magnitude and out-of-phase with the junk signal, thereby destructively interfering with it. If the Cancel signal is properly tuned, the junk signal is reduced to a negligible level compared to the power of the From Tip signal.

1.4.2 Voltage Modulated MIM

In some cases, it is useful to measure the change in MIM signal as a function of a low frequency voltage. This approach is similar to scanning capacitance microscopy (SCM) or scanning nonlinear dielectric microscopy (SNDM) [13]. In the case of semiconductors, this method can be used to determine the dopant type and relative dopant concentration [14]. In ferroelectrics, this method can differentiate between oppositely polarized domains [15].

By including a bias tee between the directional couplers and the IMN in the MIM circuit, a low frequency excitation ($0.5V_{rms}$ at 1-100kHz is typical) can be sent to the tip in addition to the usual high frequency signal. The low frequency voltage can alter the local sample properties (e.g. dopant concentration) as a function of time, changing the tip-sample capacitance and therefore affecting the high frequency impedance as a function of time. This effect is detectable by demodulating the usual MIM signal at the lower frequency using a lock-in amplifier. This is also referred to as a dC/dV measurement or voltage modulated MIM.

2 Research and Results

This section details the room temperature scanning probe hardware, the development of two types of impedance matching networks, the design and testing of our three MIM circuits, and ideas for future work.

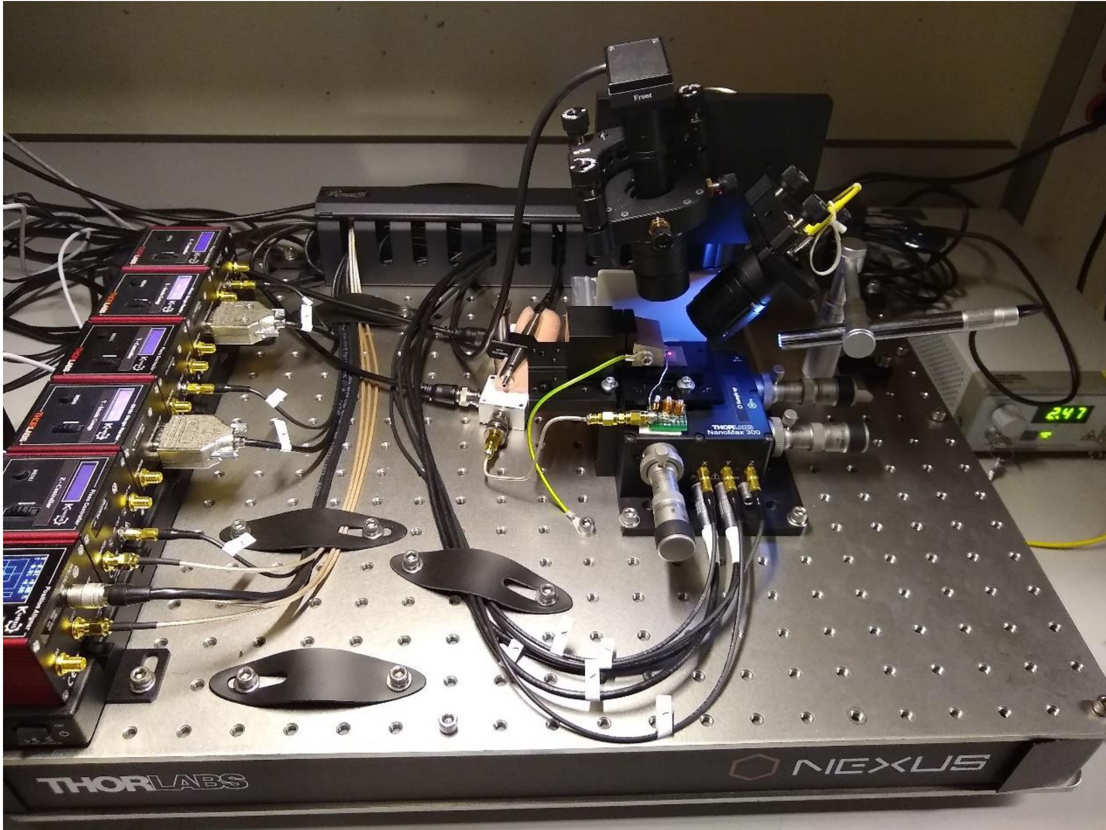

Figure 3: Photo of the tabletop AFM from Thorlabs

2.2 Tabletop Atomic Force Microscope

The tabletop atomic force microscope (Thorlabs EDU-AFM1) used for a majority of our MIM development has provided a relatively low-cost, highly modular, and physically open platform for our MIM testing (Figure 3). The atomic force microscope (AFM) components come in a kit intended for an undergraduate instructional laboratory course, so it is relatively easy to assemble and operate but only allows for contact mode measurements.

The sample sits on a flat metal stage screwed to a movable platform. Micromanipulators move the platform in three dimensions with submicron resolution. The probe is held above the sample stage by a metal clamp that is in turn fixed in place by a magnetic mount which makes removing the metal clamp to exchange probes quite simple. Piezoelectrics inside the platform can move the sample stage up to ~20 microns in each direction with roughly 20 nm resolution. Piezo controllers on the left side of the AFM platform communicate with X and Y strain gauge readers to accurately control the lateral motion of the piezos and properly account for piezo hysteresis. The Z piezo controller receives feedback from a photosensor, which monitors the deflection of the laser off the cantilever of the probe. The Z feedback loop can be used to perform constant force scans, constant height scans, and force-distance measurements. A camera mounted near the sample stage helps to align the laser with the probe and the probe with the sample.

The integration of the AFM with the MIM electronics is relatively simple. The open layout of the AFM allows the directional couplers to be fixed to the AFM platform near the sample stage, and a semi-rigid coaxial cable connects them to the IMN mounted next to the sample stage. A wire extends from the IMN and terminates in the air near the probe. By wire bonding a thin gold wire to the probe and soldering its other end to the floating wire extending from the IMN, the electrical connection between the probe and MIM electronics is completed.

The software developed by Thorlabs is a fast and user-friendly way to obtain AFM scans. It allows limited control of the scan speed and resolution with efficient X, Y, and Z feedback loops for quick and accurate stage control and topography measurement. However, it does not allow for interfacing with other software or instruments, so it is not useful for implementing MIM scans. Instead, we have developed a collection of MATLAB programs for control and readout of the lock-in amplifiers and AFM hardware to perform MIM measurements.

One significant drawback of the Thorlabs AFM is the lack of high magnification optics for aligning the sample with the probe. Regularly repeating samples, such as the Al square array

discussed in section 2.5.2, do not pose a challenge because the scan location can be anywhere within the array. However, our 2D devices are typically 10 μm on a side with 1-4 devices per wafer so locating them within the scan window becomes tedious. The location of a 10 μm scale sample relative to the AFM tip is very difficult to judge by eye, and a practiced user can only guarantee alignment to within ~150 μm if there are large, visible metallic features such as bond pads or alignment marks near the sample. We have begun depositing triangular gold features on our wafers to make sample alignment more efficient (Figure 4). Three large triangles are visible by eye and help guide the initial coarse alignment so the tip can be placed within roughly ~150 nm of the sample. Smaller, micron-scale triangles pointing toward the sample are placed in a circular field between the large triangles. If the user can get the tip in the area indicated by the three large triangles, an AFM scan will show the small triangles and point the user in the right direction. Consecutive scans allow the user to efficiently converge on the sample location.

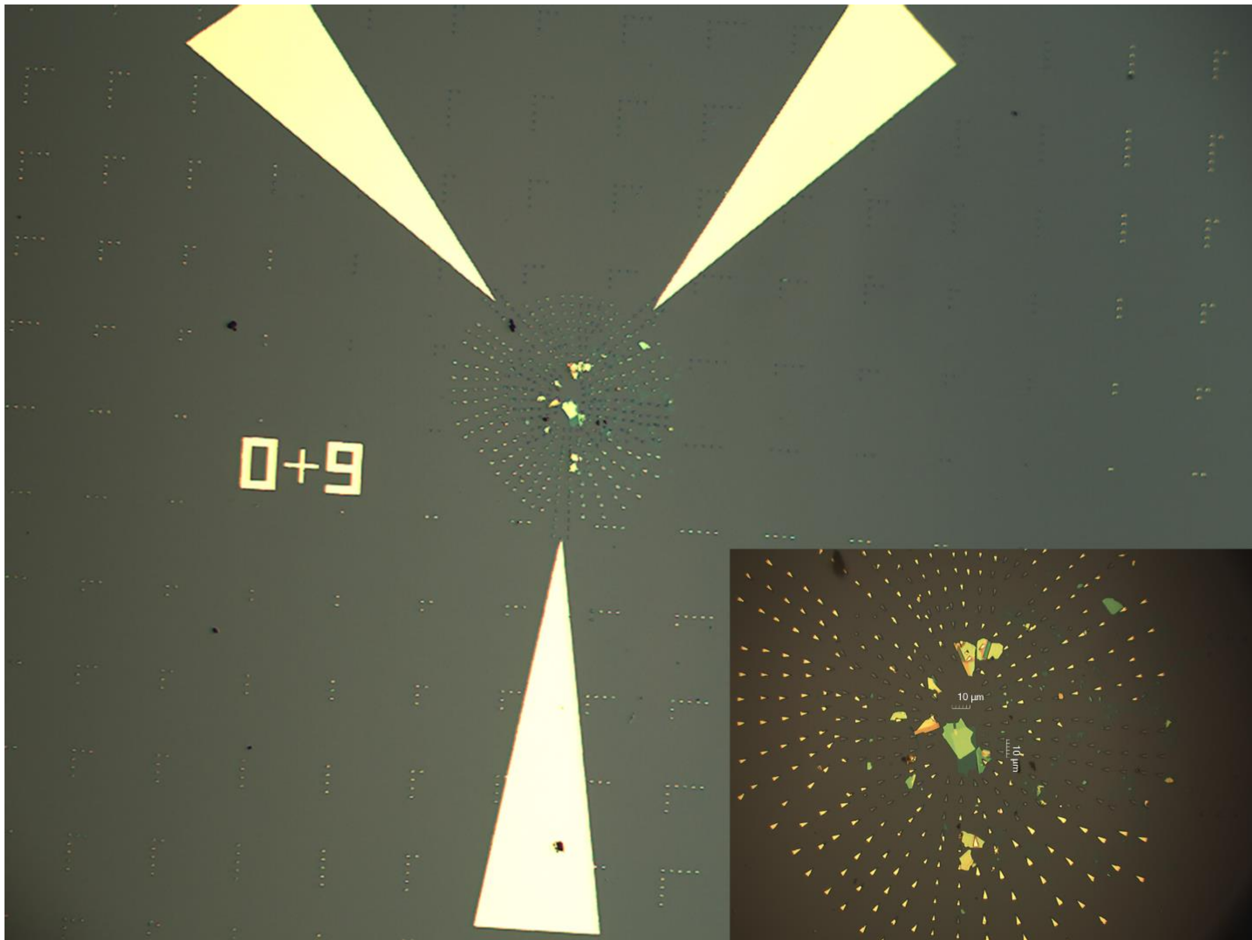

Figure 4: Large triangular gold markers for visual alignment of the AFM tip. Inset: Magnified view of the sample region showing smaller gold triangles for alignment via AFM imaging.

2.2.2 MIM Probes

The choice of probe for MIM measurements is critical to the success of an MIM measurement. Dull or broken probes can limit the resolution and lead to imaging artifacts as is the case for any SPM technique. Additionally, MIM measurements are sensitive to the entire probe geometry and the probe's physical environment. For example, large bonding pads can create a significant parasitic capacitance, so it is necessary to ensure proper shielding, minimize the size of the bonding pad, or eliminate the bonding pad altogether.

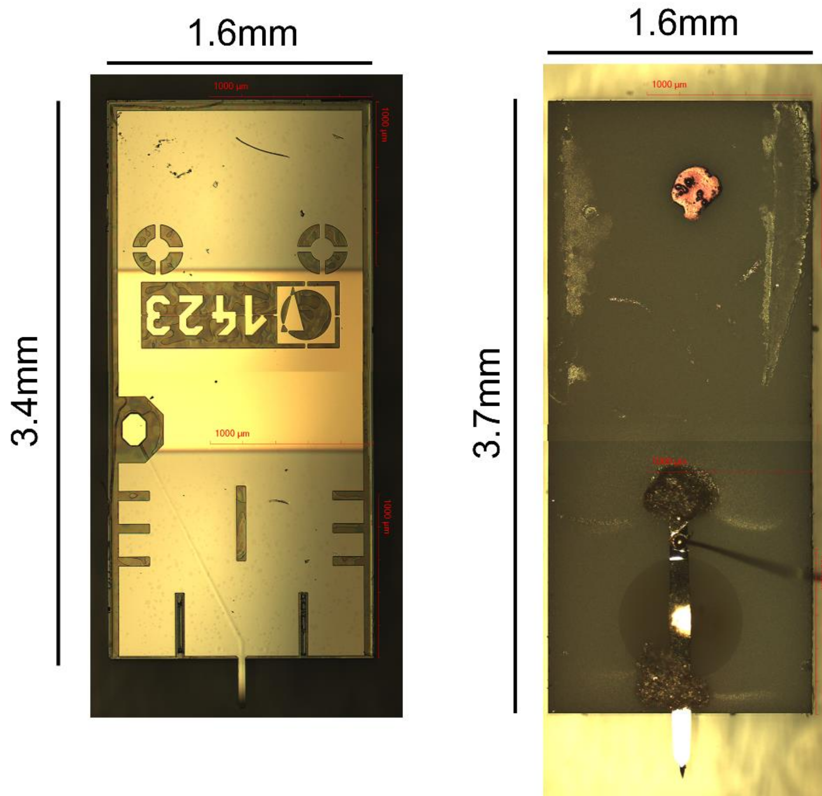

Figure 5: PrimeNano long probe (left) and RMN 25Pt300C probe (right). The PrimeNano probe's small octagonal bond pad the left side is linked by a buried metallic path, faintly visible in the image.

Most of our testing has been performed with Rocky Mountain Nanotechnology's 25Pt300C probes (Figure 5). These are a variation of their 25Pt300 series probes without a bonding pad. Their relatively long tip length (80 μm) also keeps the cantilever far from the sample and minimizes stray capacitances. They are relatively stiff with a spring constant of 18 N/m, and we have plans to test model 12PtIr400C as a replacement. This newer model is made from a PtIr alloy for increased durability, and it has a low spring constant of 0.6 N/m which will be gentler on our 2D samples.

We also performed a short series of tests with PrimeNano's Long probes (Figure 5). These probes forgo the long tip shank of the RMN probes in favor of metallic shielding. A thin metallic strip surrounded by silicon nitride links the 5 μm tip to a small bonding pad near one edge of the probe body. A metallic outer layer provides electrical shielding and a reflective

surface for laser feedback. These probes have a low spring constant (1 N/m) making them suitable for contact mode MIM, but tests with two of these probes demonstrated that they can affect the frequency and quality of the impedance match so switching between PrimeNano and RMN probes can require tedious retuning of the IMN. Given that RMN probes are cheaper and seem to provide a more reliable impedance match, we typically opt for RMN probes over PrimeNano probes in our room temperature MIM tests.

2.2.3 Modification for Chip Carriers

Many of our samples are mounted on leadless chip carriers (LCCs) for transport tests, so it is useful to have electrical connections to a sample during MIM scanning. The standard sample stage has a flat surface, so we designed a method of firmly mounting an LCC socket in place of the sample stage (Figure 6).

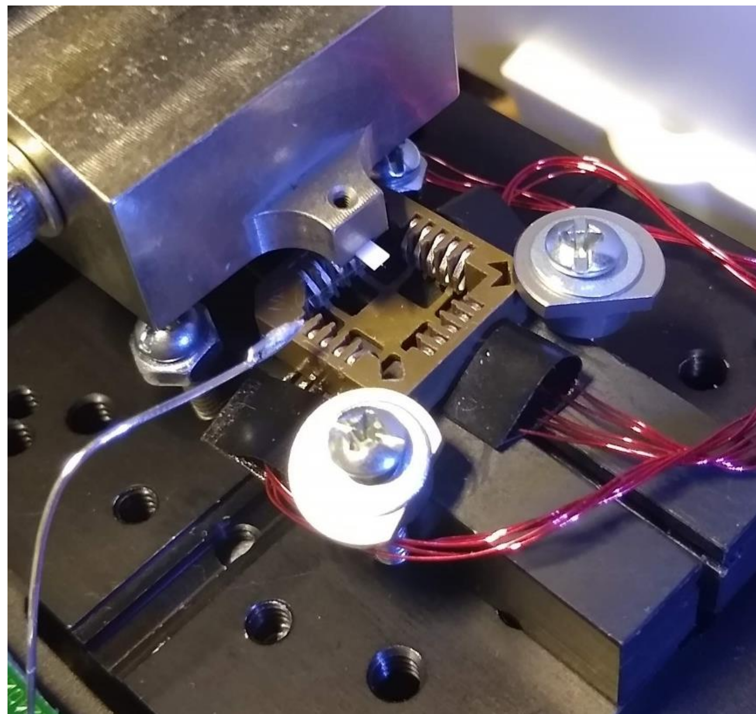

Figure 6: The LCC socket mounted on plastic pieces for height and held in place by screws.

The sample stage must be removed from the piezo controlled platform to make additional screw holes available and leave enough space beneath the probe holder for the socket. Two long plastic rectangular prisms are placed in the center of the platform and held in place with two screws. Two more screws hold a low-profile LCC socket on top of the plastic pieces. The placement of the screws is such that they do not hit the probe holder, which extends horizontally over the plastic pieces and socket. The socket has 20 pins on its underside, which are bent outward for wires to be soldered in place. The wires connect the socket to a breakout box with 20 BNC ports for easy connections to measurement electronics.

The socket is relatively short, but a sample wafer mounted on a chip carrier and inserted in the socket is too low for an AFM tip to reach. The underside of the probe holder hits the edge of the socket before the tip hits the sample. To address this, 4 spare silicon wafers must be mounted firmly on the chip carrier (typically with PMMA or silver paint) before the sample wafer is mounted on top, leading to an awkwardly tall stack. The bonding wires must traverse this step height to connect the sample at the top of the stack to the contacts around the perimeter of the chip carrier. Additional care must be taken when choosing the orientation of the sample wafer relative to the chip carrier to minimize the number of bond pads on the side of the sample covered by the probe holder. The probe holder gets close enough to the wafer surface that it could touch gold wires connected to these bond pads, causing them to short to ground or break off. Minimizing the loop height during wire bonding also helps to avoid this issue.

2.3 Impedance Matching Networks

2.3.1 λ/2 IMN Design

This IMN design was copied from the Shen group (Figure 7) and consists of a small capacitor and a length of coaxial cable cut to half the wavelength of the first harmonic. The

signal travels at 0.7c in the PTFE dielectric, so to target a fundamental mode near 1 GHz the coaxial cable was cut to about 10 cm (v = λf). The S11 responses of many IMNs were tested with a vector network analyzer. Ideally, the network analyzer would show a dip in power >10 dB deep with a FWHM of <30 MHz near 1 GHz and at higher harmonics (2 GHz, 3 GHz, etc.). The observed S11 profile was highly dependent on the following: the capacitance value, the cable lengths, whether a probe was attached, a person's physical proximity to the IMN during testing, the length of the exposed inner conductor of the coaxial cable, the quality and shape of the solder connections, and the flexibility of the coaxial cable.

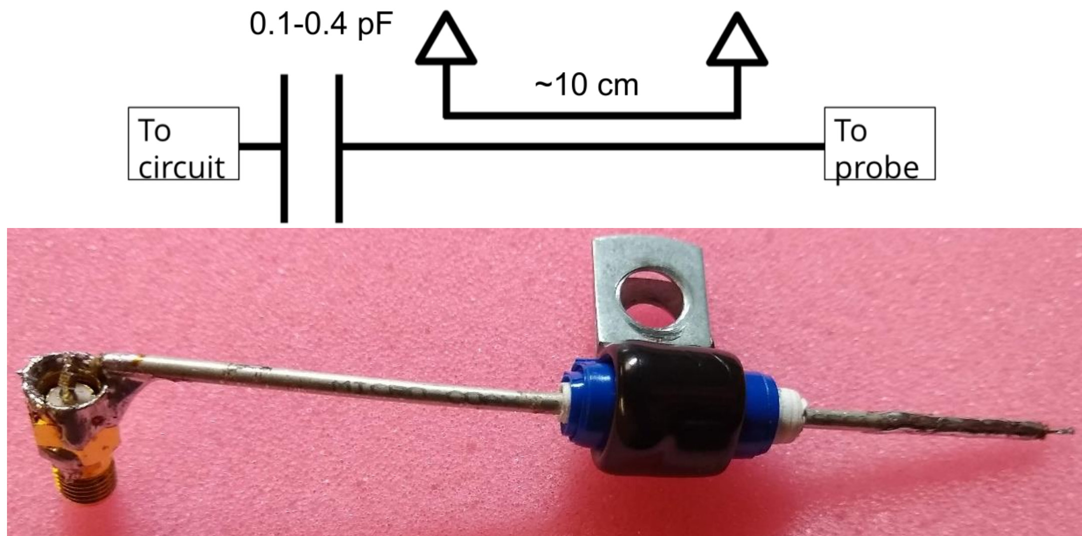

Figure 7: Diagram of λ/2 IMN (top) and example image (bottom)

It was found that the best match to the cantilever-style probe typically uses a 0.1 or 0.2 pF capacitor with a 10cm semi-rigid cable and an inner conductor extending from the coaxial shield <5 mm on either end.

The presence or lack of high-quality resonances is extremely dependent on whether a cantilever-style probe is connected. A λ/2 style IMN may appear to have no resonances at all, until the cantilever is connected, or it may appear to have good resonances that disappear entirely after the probe is connected. This does not appear to be a problem with thin wire probes or with the IMN design used for MHz imaging.

Adding a 500 kΩ resistor in parallel to the capacitor is necessary in principle for dC/dV or DC offset measurements using this type of IMN. However, it can affect the quality of the match, so it is usually omitted when regular MIM is the goal.

The choice of semi-rigid cable in the IMN for room temperature measurements was based on observations that flexible components included in the circuit between the directional couplers and the AFM probe greatly increase noise at room temperature. It is likely that this consideration is less relevant for cryogenic systems, because most flexible components become stiff at low enough temperatures anyway.

This same type of IMN is used with the 2-10GHz circuit which offers the flexibility of choosing from the matching at any harmonic. The quality of the match at each harmonic usually varies, so being able to choose the harmonic with the best matching is convenient. See Figure 8 for an example frequency sweep using the 2-10 GHz circuit.

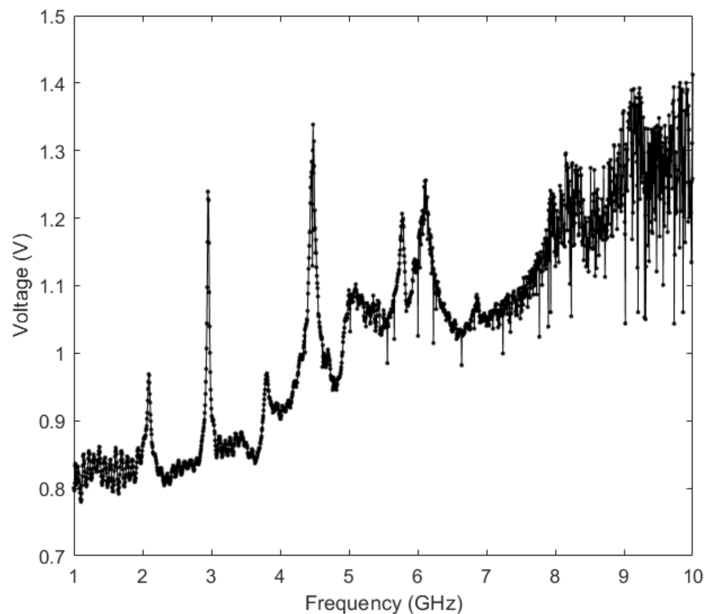

Figure 8: Example frequency sweep obtained with the 2-10 GHz circuit using a λ/2 IMN. Note the quality of the match at each harmonic varies.

A longer length of coaxial cable lowers the fundamental frequency and reduces the spacing between each harmonic, which provides more harmonics to choose from in a given range but above 10-20 cm the cable length becomes difficult to support and soldering to it becomes much harder due to the increased thermal mass. The gold wire melts at temperatures much above 200 C, which is also near the lowest temperature setting for some soldering irons and close to Sn/Pb solder's melting point. Longer cable lengths take much longer to heat enough to melt the solder, much longer to cool down, and it appears contact with the larger thermal mass also increases the chance of the gold wire melting. A mechanically tunable capacitor is a convenient alternative to a fixed value capacitor because they allow fine tuning without the need for soldering, but they are hard to find in the right values and sizes for the λ/2 style IMN.

2.3.2 MHz IMN Design

The IMN used with the MHz circuit is also based on a design from the Shen group and doesn't use any coaxial cable (Figure 9). A variable capacitor, typically in the range 2-10 pF and several tunable inductors roughly 100 nH each are soldered to a prototyping board, along with an SMA connector and a length of exposed wire. Changing the inductance by removing or adding inductors or by changing the depth of their removable aluminum cores shifts the matching frequency, with a larger inductance resulting in a lower frequency. When tuning by means of the aluminum core, the minimum inductance is achieved when the core is fully centered in the coil, and the maximum inductance when the core is fully removed. Tuning the capacitor primarily affects the quality of the matching resonance.

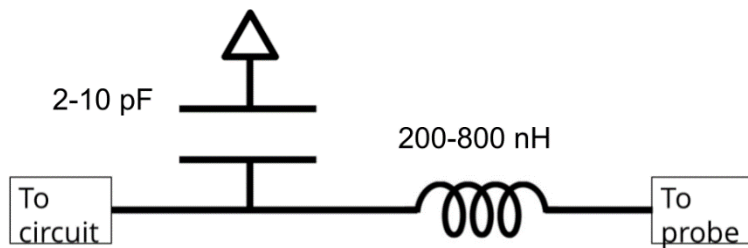

Figure 9: The MHz IMN diagram (top) and picture (bottom).

2.4 1 GHz Circuit

2.4.1 Development

The 1 GHz MIM circuit is based on a design from the Shen group at Stanford University (Figure 10). It is more complex than that of the 2-10 GHz circuit, with the advantage that calibration and measurement can be fully controlled by a computer. It operates in a narrow frequency range near 1 GHz and contains more filters and an additional attenuator compared to the other designs (Figure A.1). As the first completed MIM circuit, troubleshooting the 1 GHz

setup also required testing and troubleshooting of the impedance matching method and the scanning hardware.

The 1 GHz circuit requires a separate power supply, a dedicated microwave source, two voltage pre-amplifiers, and DC voltage sources and readout (Figure A.2). An SR830 lock-in amplifier with four analog inputs and outputs meets the latter requirement. Its lock-in capability is useful for dC/dV imaging as well.

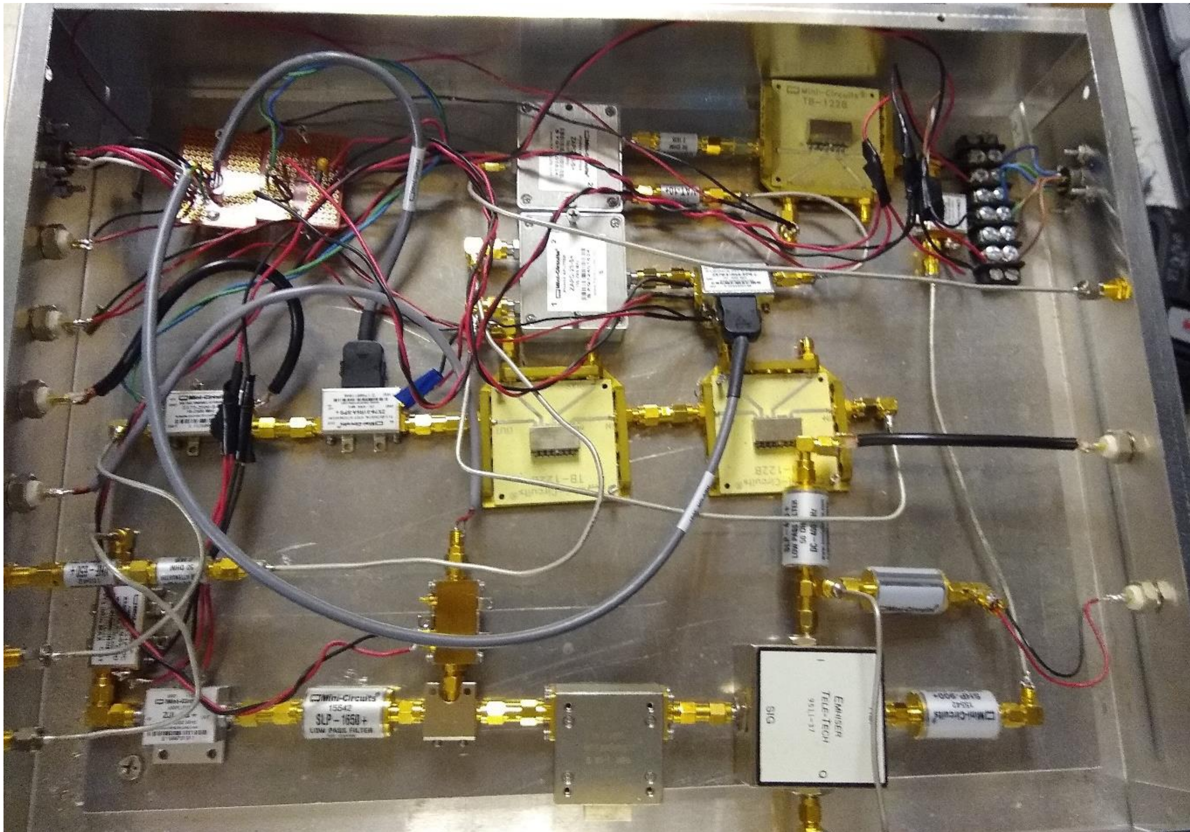

Figure 10: Image of the 1 GHz MIM circuit

2.4.2 Initial Testing

The first tests of the 1 GHz setup focused on making an IMN with a reliable impedance match from the 50 Ω cable impedance to our MIM probes as described in section 2.3.1. After obtaining a good impedance match near 1 GHz it was necessary to check that the matching resonance was observable with the MIM circuit and to test the calibration of the Cancel signal.

The 1 GHz circuit uses an RF-to-DC power monitor which converts the total power it receives across its operating range into a DC voltage. The DC output is inverted relative to the measured power, so the maximum reading, 2 V, indicates the unit is measuring no RF power and the minimum reading, 0.5 V, indicates the unit is fully saturated (Figure 11). Sweeping the output frequency of the microwave source and measuring the power monitor voltage, a peak in the

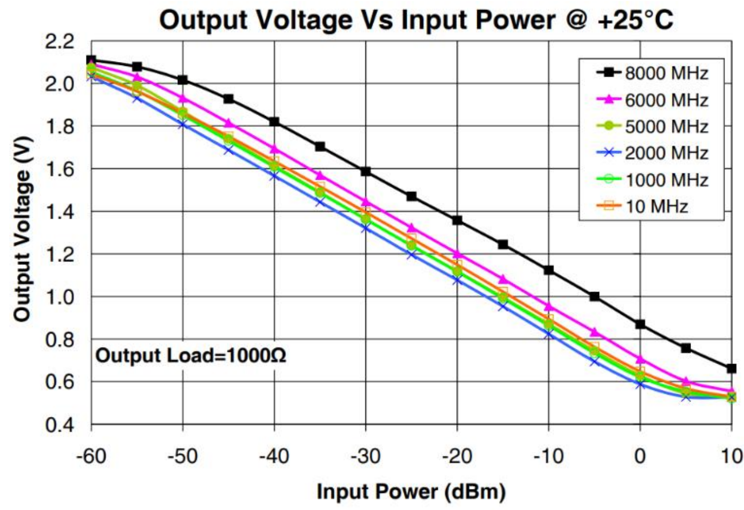

Figure 11: RF power to DC voltage relation for the power monitor in the 1GHz circuit (from minicircuits.com)

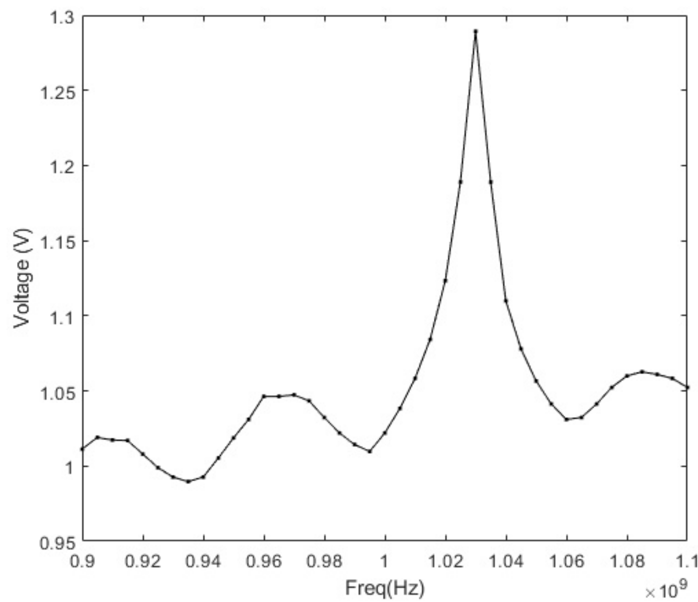

Figure 12: Example frequency sweep using the 1 GHz circuit to identify the matching resonance of a λ/2 IMN

signal indicates a low reflected power and therefore good impedance matching (Figure 12). Sweeping the cancellation phase and attenuators also shows a peak in the power monitor signal where good cancellation occurs.

Early tests also showed errors in the MATLAB control of the two digital attenuators. One of the attenuators is included in the Cancel portion of the circuit to act as a coarse adjustment for the magnitude of the Cancel signal, and the other is located before the power divider that splits the Measurement signal into the To Tip and Cancel signals. This second digital attenuator is not present in the other circuits, but it can be useful to reduce the overall signal received by the amplifiers to prevent them from saturating, without affecting the overall balance between the To Tip and Cancel signals. The digital attenuators are controlled by an Arduino which receives commands from a MATLAB program. The Arduino is connected to the attenuators by several wires which the attenuators have in common, and one unique wire each. These wires unique to each attenuator deliver the Latch Voltages, which instruct the attenuators to accept or ignore input. One of the common wires carries the Command Voltage, which encodes the commands to change attenuation. The other common wires provide grounding and clock signals that are not relevant for typical operation. Because the Command Voltage is delivered by a common wire, it is always received by both attenuators regardless of which attenuation is being changed. This makes it important to properly enable and disable the latch, so the right attenuation is changed. The original program for controlling the attenuators did not account for this, so both attenuators would change to the same value every time a change command was sent. It was determined empirically that the latch for each attenuator is enabled as soon as the corresponding attenuator variable is defined by MATLAB. To ensure that a given attenuation does not change after the right value is set, it is necessary to clear the MATLAB variable to disable the latch before defining and commanding the other attenuator. Even after implementing this change, tests with a vector network analyzer demonstrated that occasionally the commands sent to the attenuators were not interpreted correctly, and the attenuators would sometimes

change to incorrect values, even with a closed latch. It was eventually determined that the bitrate chosen in the original MATLAB program was set too high (5,000,000 bits/s) and a lower value (25,000 bits/s) provided reliable control.

For several months we used RMN 12Pt300B and 25Pt300B models, which both had large gold bond pads (Figure 13). At the suggestion of Professor Yong-Tao Cui from UC

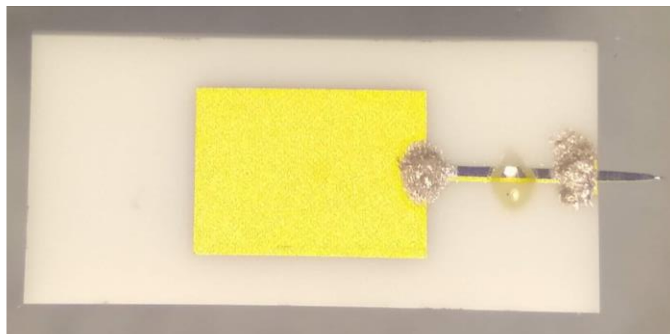

Figure 13: RMN probe with a large gold bond pad

Riverside who worked extensively on MIM with the Shen group, we switched to 25Pt300C model probes which are not advertised by RMN. These are identical to the 25Pt300B model but without the gold bond pad which can cause a problematic stray capacitance.

The cryogenic amplifier (Cosmic Microwave Technology, Inc. model CITCRYO01-12D) was also seen to be a significant source of noise. We tried several methods of sourcing power to the amplifier with limited success until finally purchasing a dedicated DC voltage regulator from the amplifier vendor and visiting the vendor in person for detailed notes and instruction on its operation (Appendix C). The voltage regulator requires +5 and -5 V DC sources as input and contains filters to prevent noise from the power supply from affecting the RF signal. The vendor provided a spec sheet showing the measured noise at room temperature and at 12 K before they shipped the amplifier and their values at room temperature were significantly below the noise observed by our power monitor. The amplifier operates across 1-12 GHz and the range of the power monitor spans 0.01-8 GHz, so the noise at room temperature is likely a result of the power monitor aggregating all the noise across its operating range to output a single noise

value. We purchased a 1 GHz bandpass filter (RF Bay BPF-950L) to help mitigate this issue, but additional testing is needed to confirm its effectiveness.

Currently, our best results with the 1GHz circuit have been obtained using probes without bond pads, with the updated attenuator control code, and without including the cryogenic amplifier. After careful tuning of the Cancel signal with the tip floating above the sample, the sample is raised to contact the tip and the MIM response increases dramatically, which is expected for a working system. However, subsequent scanning only showed a response correlated with the motion of the sample stage, not local electrical properties (Figure 14). The system was also highly sensitive to the locations and motion of nearby people and objects. This sensitivity is observed to a lesser degree with the MHz and 2-10 GHz circuit, which show a response to motion within about 1 m of the system. The 1 GHz system showed a response correlated with motion up to about 6 m away, and occasionally farther.

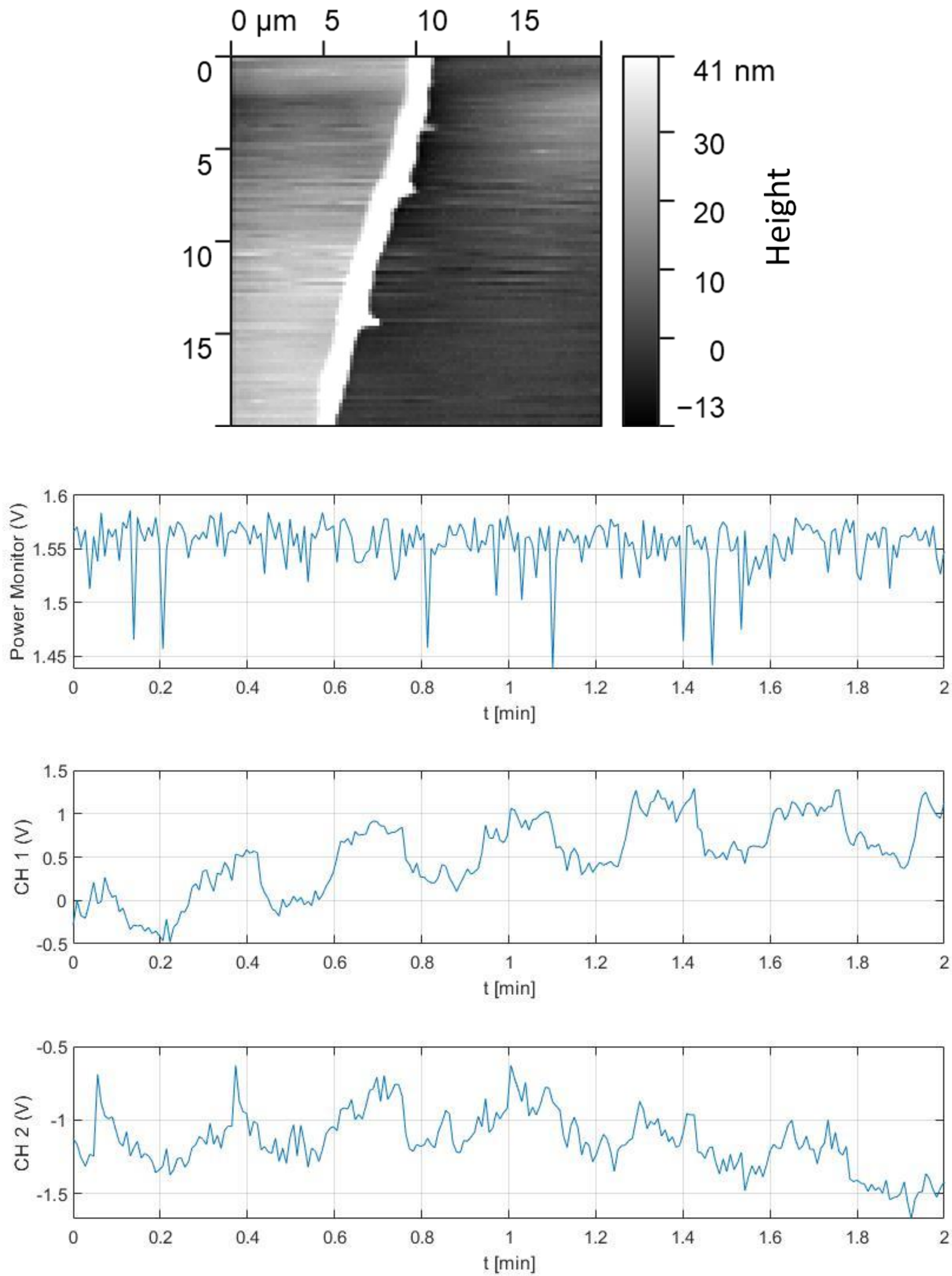

Figure 14: Top: AFM image of a graphite flake (left side) on bare SiO2 (right side). Bottom: MIM data recorded as the sample was scanned horizontally. The CH 1 and CH 2 data show repetitions that correlated with the motion of the stage, not the material the tip was in contact with. All three signals are relatively noisy.

To determine whether the problem was in the MIM circuit or somehow related to our scanning hardware, we performed additional tests using the Veeco SPM in the Nano3 user facility instead of our Thorlabs AFM. We were allowed one full day to integrate our 1 GHz electronics and perform tests on various samples including graphite, hBN encapsulated graphene, and hBN covered Au features. Again, the MIM response correlated with the sample motion but not the local sample properties, leading us to conclude that the issue is in the 1 GHz circuit.

Near the end of the 1 GHz circuit tests, we noted that the original circuit design from Stanford included a high-pass filter (Mini-Circuits SHP-900+) before the Ref input of the mixer, whereas our design used a low-pass filter (Mini-Circuits SLP-1000+). Both filters included the frequency range around 1 GHz and should not have been filtering out the relevant signal at 1 GHz, but it is possible that a spurious low frequency signal was interfering somehow. The high-pass filter from the original design was purchased and installed instead, but at that point we had begun achieving success with the MHz circuit. It is hoped that having replaced the low-pass filter on the Ref port of the mixer with the high-pass filter and adding the 1 GHz bandpass filter to the output of the cryogenic amplifier will combine to make the circuit function properly, but as of the time of writing this circuit has not been proven to work.

2.5 MHz Circuit

2.5.1 Development

The 10-200 MHz MIM circuit was developed in response to the challenges that arose in testing the 1 GHz circuit (Figure 15). The combination of frequency source, reference line, and mixer in the RF lock-in simplifies the circuit significantly, making it easier to construct and troubleshoot (Figure A.3, Figure A.4). RF components in the MHz range are also much cheaper

and easier to source. The calibration and measurements are fully controlled by the computer, like the 1GHz circuit, giving it an additional advantage over the 2-10 GHz box.

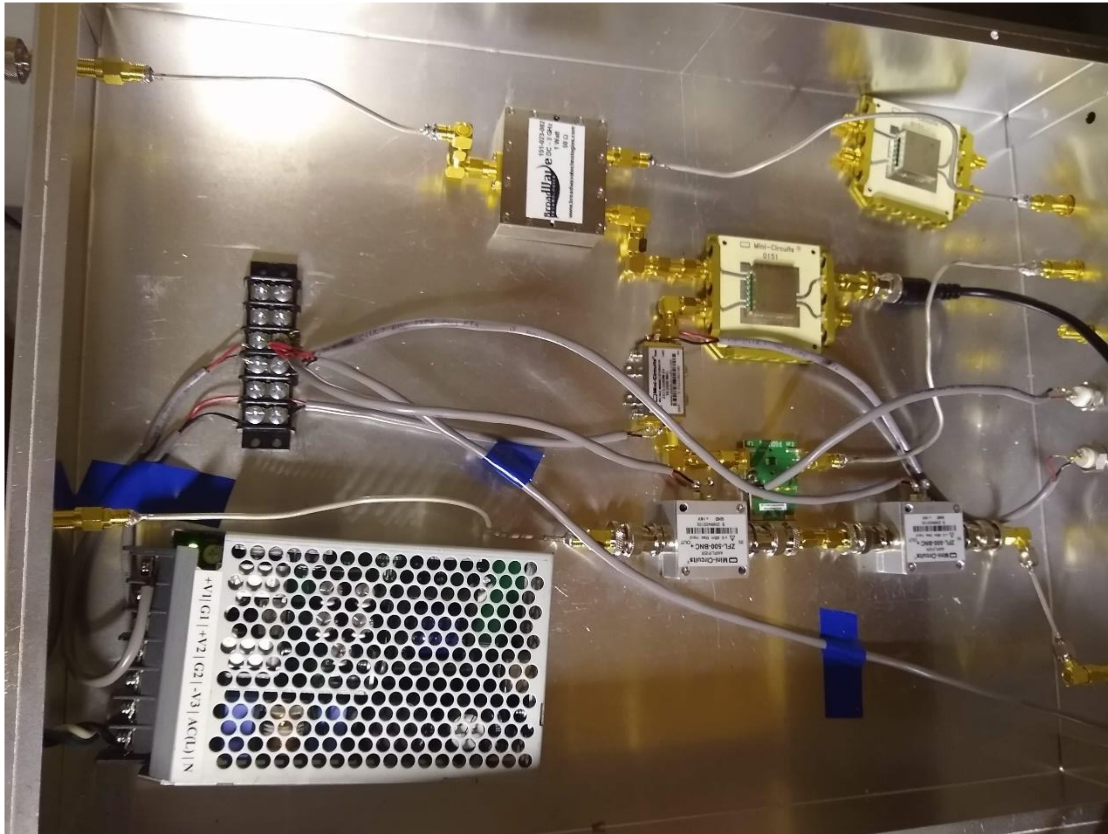

Figure 15: Image of the MHz MIM circuit

2.5.2 Initial Testing

Preliminary tests with the MHz circuit used the Thorlabs AFM hardware but we still had not developed 2D scan control, so MIM data were recorded as a function of time while the tip scanned across adjacent insulating and conducting samples. We briefly explored methods to wrap the data to create 2D color plots, but the resulting images were significantly distorted (Figure 16b). By modifying a MATLAB library used previously by our postdoctoral researcher, Rajarshi Bhattacharyya, we were able to send commands to the piezo controllers to change the sample position and generate spatially resolved plots.

Early tests demonstrating successful operation were performed on a graphite sample on a SiO_2 substrate. The high conductivity of the graphene sample provided good contrast with the insulating substrate, but the resolution was poor, and the images lacked detail (Figure 16c).

More tests were performed on a series of 5 μm x 5 μm aluminum squares 100nm thick deposited in an array on SiO_2 (Figure 17). The highly regular pattern of Al squares over a large area made locating a specific sample irrelevant and saved time in repeated tests. At this point it was observed that using two amplifiers in the From Tip line instead of one improved the signal to noise ratio and improved image quality. Ensuring that the directional couplers sitting on the AFM platform were firmly held in place and using semi-rigid coaxial cable to connect them to the IMN also significantly reduced noise.

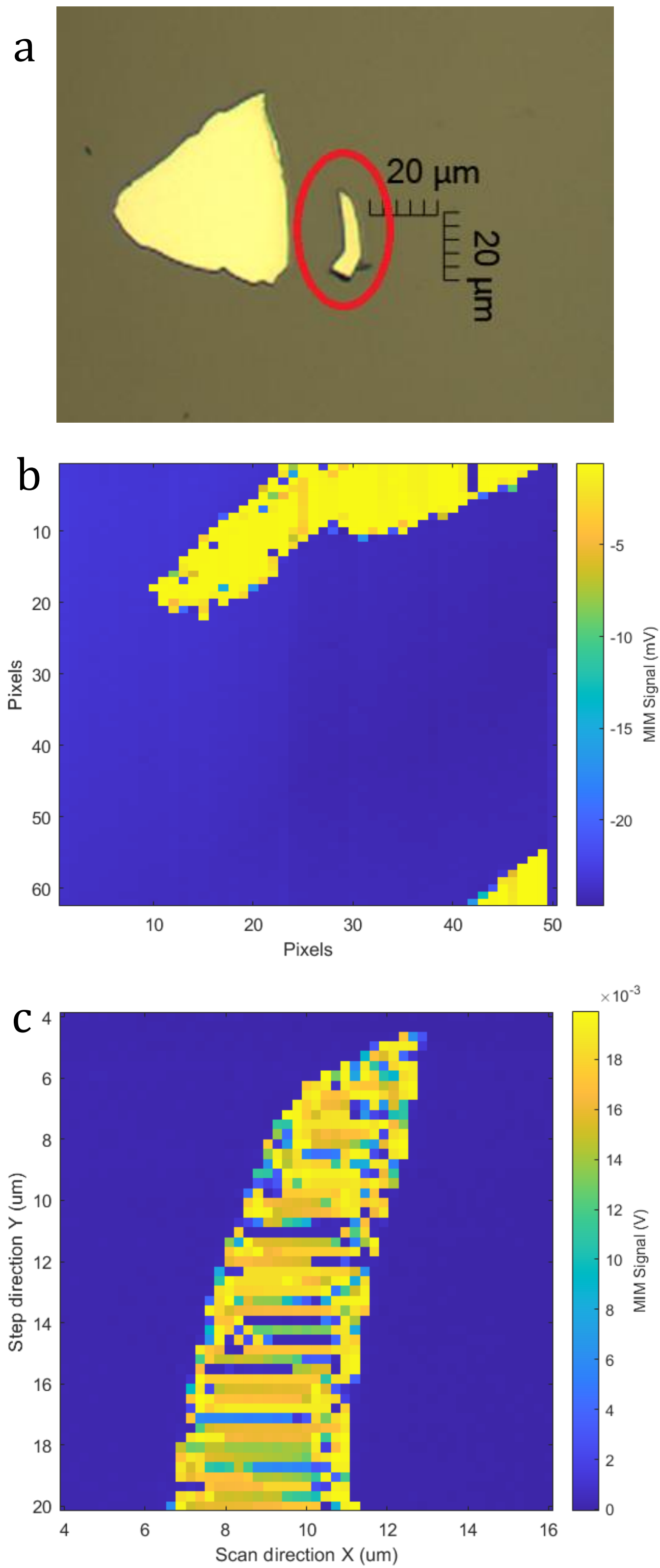

Figure 16: Early MIM scans of graphite. a) Optical image of the graphite flake. b) MIM data taken as a function of time and wrapped to generate a 2D color plot. c) MIM data recorded after modifying the scanning software to send commands to the X- and Y-piezos.

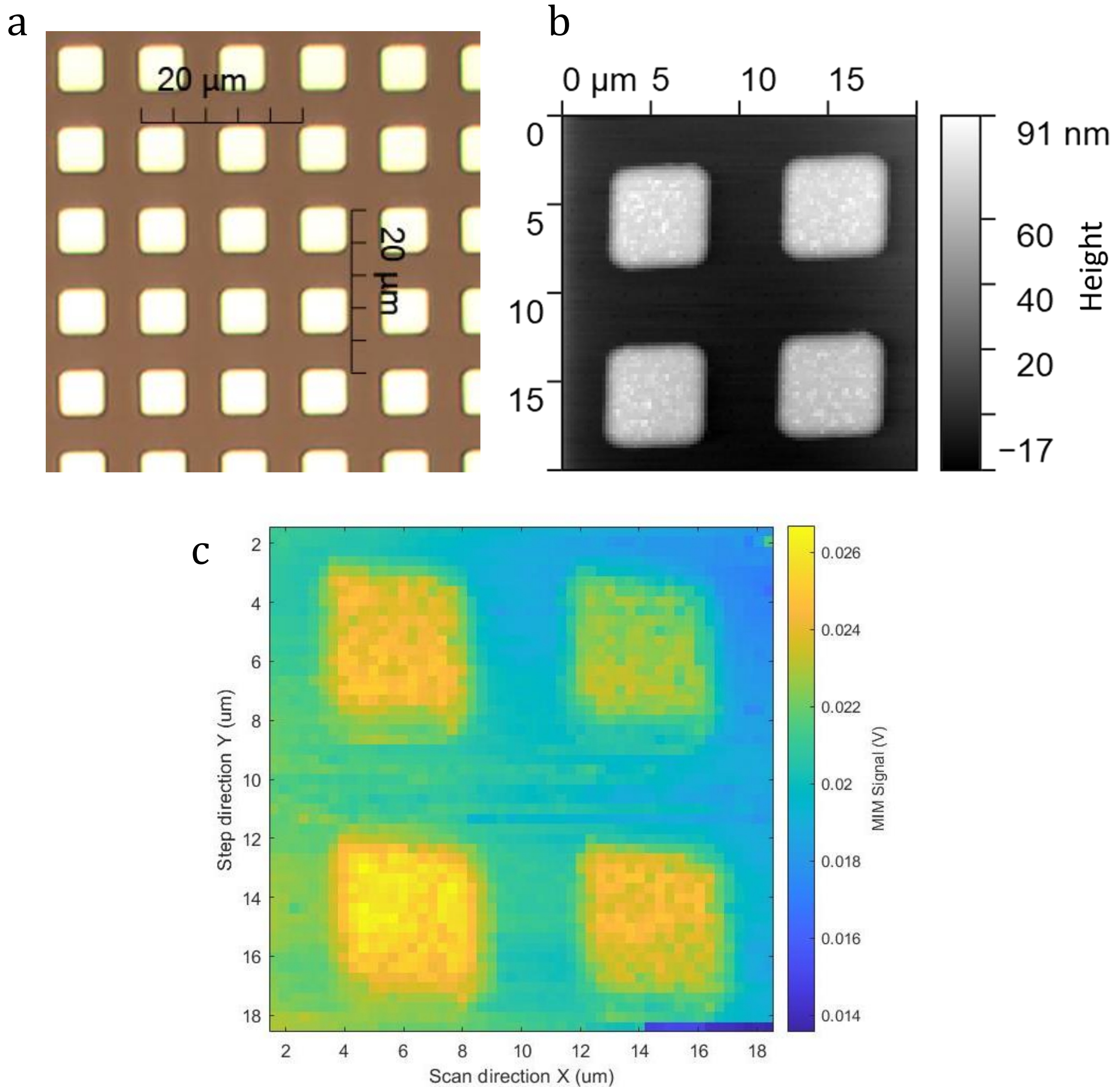

Figure 17: (a) Optical, (b) AFM, and (c) MIM-Im images of aluminum squares on SiO2

To better characterize the MIM's performance, arrays of finely spaced gold rectangles intended for use as back gates were imaged. In full area scans (20 µm x 20 µm) the gate arrays were evident, but resolution was poor and the gaps between the gates (150-200 nm) were not observed (Figure 18a). Executing smaller area scans to decrease the area per pixel and resolve the gaps instead yielded images with significant distortions (Figure 18b). The data appeared to

contain minor horizontal shifts in scans below roughly 10 μm x 10 μm in size, and scans below 5 μm x 5 μm showed serious warping. We attributed this to a shortcoming of our piezo control program, which was only able to set the X and Y piezos to a specific voltage calculated from a rudimentary conversion between voltage and position. The program did not read the strain gauges to determine the true location of the sample, so the images were susceptible to drift and hysteresis in the piezos. This was addressed in a later update of the control software and will be discussed in section 2.5.3.

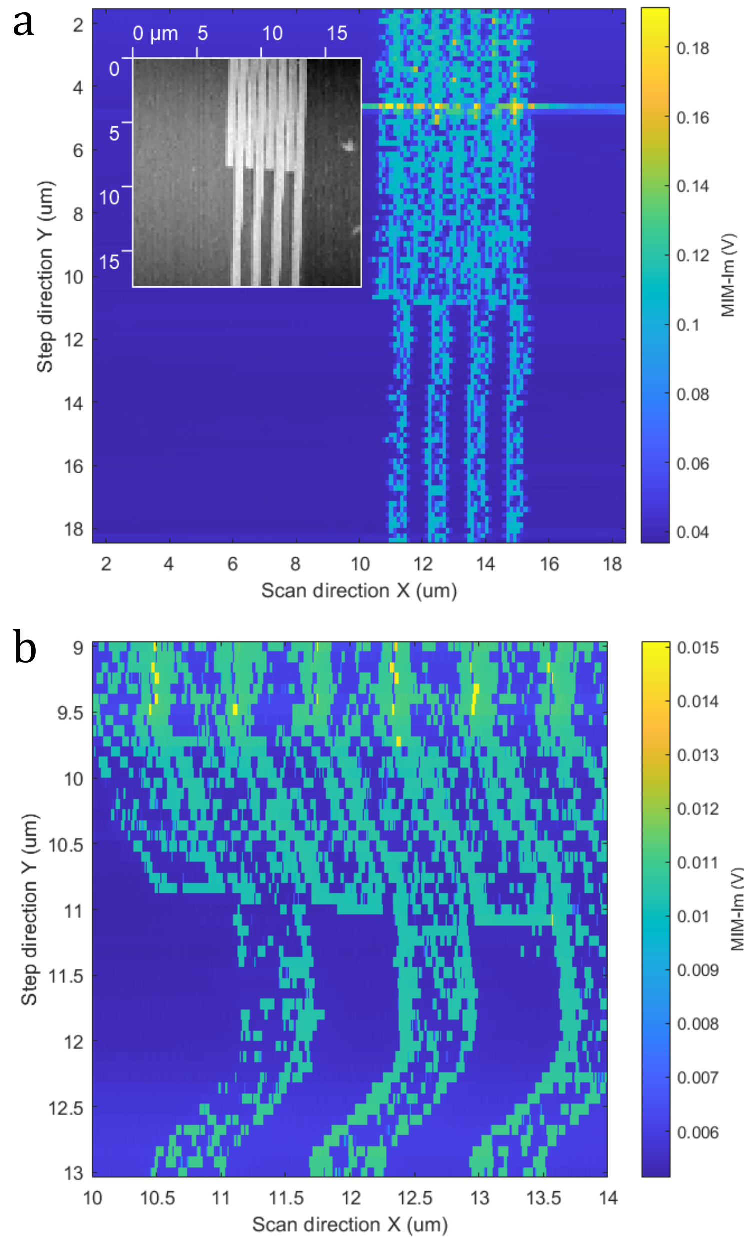

Figure 18: MIM images of gold rectangles. a) Wide area scan. Inset: AFM image of gold rectangles. b) Small area scan showing warping from piezo hysteresis.

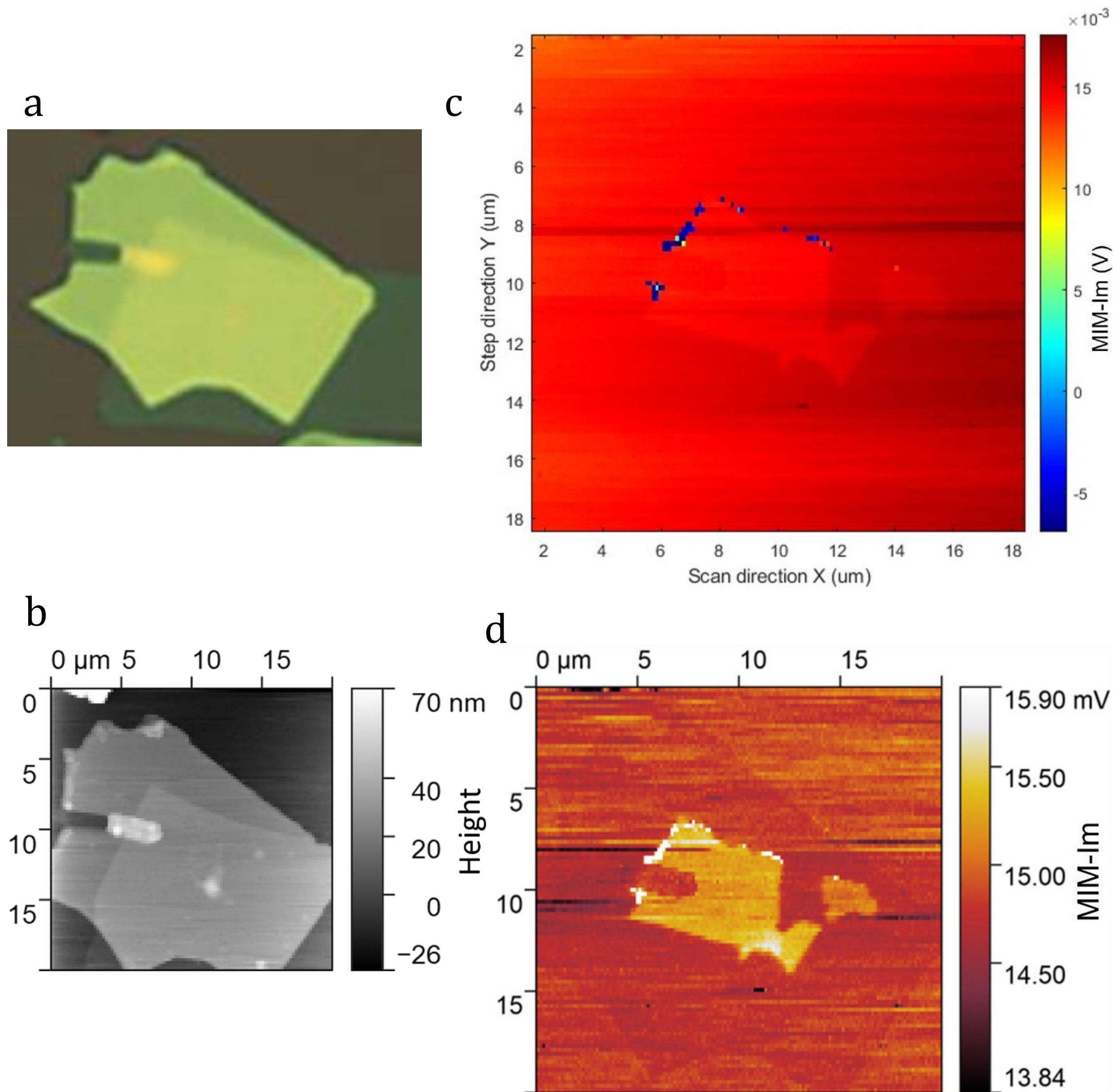

Figure 19: Encapsulated twisted bilayer graphene. a) Optical image. b) AFM image. c) Raw MIM image. d) MIM image after editing in Gwyddion to improve the contrast.

To test the sensitivity of the MIM to subsurface features, a bilayer graphene flake encapsulated in hexagonal boron nitride (hBN) was imaged (Figure 19). Initial images contained a few sharp spikes and dips where the MIM signal was unusually large (possibly due to unusual surface features or measurement noise) so the color scale was artificially expanded and the

contrast between the graphene and hBN regions was poor. By developing a short program to convert the MATLAB data to a .csv format, it became possible to import the raw data into the Gwyddion SPM data analysis software. Gwyddion enabled correction of the color scale by eliminating the hot pixels, the encapsulated graphene region became evident, and we confirmed the subsurface imaging capability of the MIM.

The final test to characterize the MHz MIM imaging capabilities sought to observe a Moiré pattern on exposed twisted bilayer graphene on hBN. The rotation angle between the two graphene layers leads to a Moiré pattern which, depending on the angle, can have a length scale up to tens of nanometers. Previous work had observed Moiré patterns in twisted bilayer graphene and in monolayer graphene on hBN with nanometer-scale resolution using MIM. Our large area MIM images showed distinct contrast between the graphene and hBN regions, but no Moiré pattern was observed. Small area, high-resolution scans similarly did not show any Moiré-like structure and were likely affected by the hysteresis-caused warping observed in the gate array tests. Additionally, the graphene region appeared to change shape and shrink with consecutive scans, demonstrating that the tip was damaging the fragile graphene surface and scratching it away (Figure 20). Steps have since been taken to mitigate tip damage and will be discussed in section 2.5.3. This concluded our initial series of tests to characterize the MHz MIM circuit in conjunction with the Thorlabs AFM.

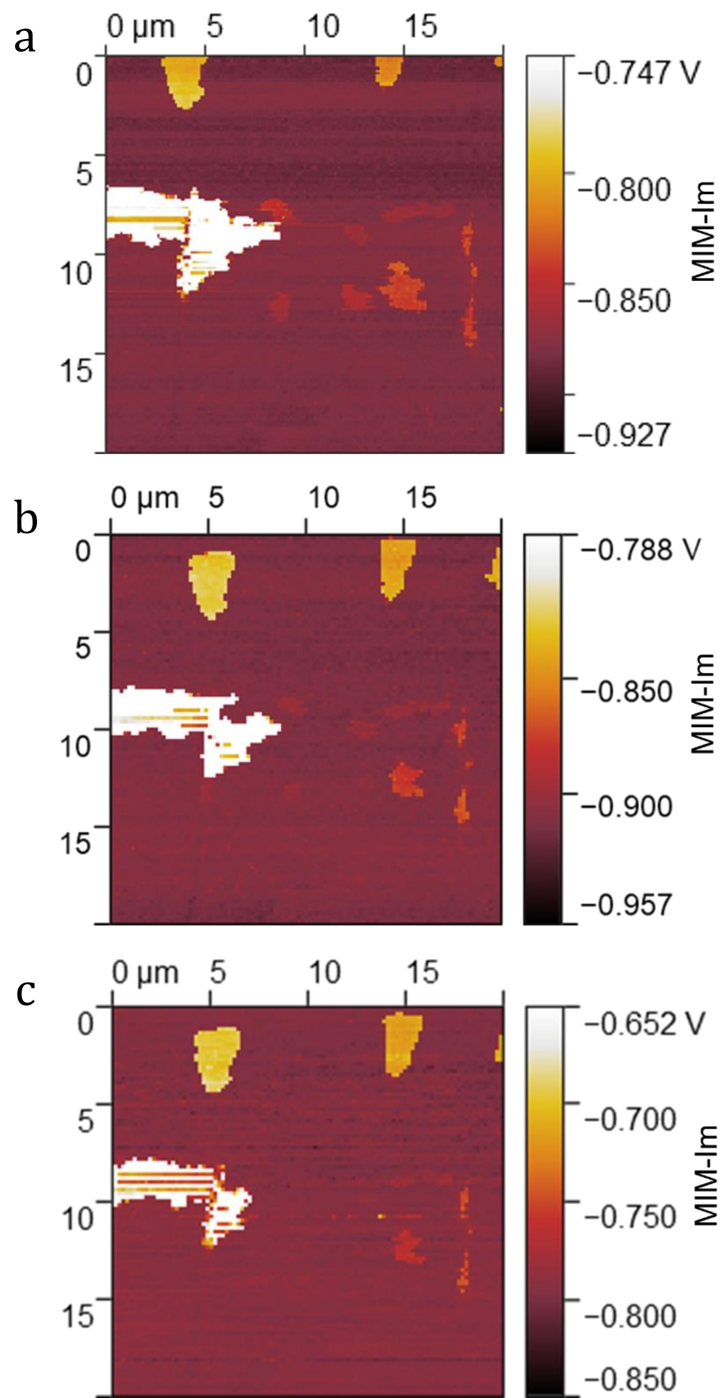

Figure 20: Consecutive MIM images showing gradual destruction of an exposed graphene flake (white) and nearby gold alignment marks (yellow) on an SiO2 substrate (red)

2.5.3 Further Improvements

The early version of the scanning software assumed that the full voltage range of the piezo controller (0-75 V) corresponded to the full range of motion of the piezo (0-20 μm). To scan the sample, the measurement area and density of pixels was chosen, and the proper locations computed. Using the 75 V / 20 μm conversion, the piezo controller was directed to apply the voltage corresponding to the next location, the MIM data was recorded, and the process was repeated. This led to global positioning errors up to ~1 μm in magnitude and an image warping effect caused by drift and hysteresis in the piezo when the scan area was small.

Documentation from Thorlabs outlined commands that would enable communication with the strain gauges for accurate positioning, but the syntax appeared incompatible with MATLAB. When focus later shifted from validating basic MIM operations to improving its capabilities, a discussion with Thorlabs clarified the proper syntax and an updated scan control program was written. The updated program still broke the scan area into discrete target locations but when moving between locations it iterated between setting the piezo voltage and reading the strain gauge reader to accurately arrive at the destination. The initial guess for the correct piezo voltage was informed by the distance between the starting and target locations. A larger distance would result in a larger voltage increment to dynamically approach the target location and prevent large position changes from taking significantly longer. The strain gauge would then read the new location and the program would make a correction to the applied voltage, iterating this process to arrive at the target. When the strain gauge reported a position within a predefined tolerance of the target position, the process would terminate. A damping term was also introduced to limit the size of the voltage changes and avoid overshooting the target location. This feedback approach led to positioning accuracy on the order of the strain gauge resolution (~3 nm) and took about 1 s to approach most locations. However, this program required careful calibration of the strain gauge readers because negative voltage or strain

readings caused errors in the approach loop. Even if the hardware was calibrated correctly, a significant delay in approaching positions near 0 μm in either dimension was observed, meaning scans including these locations took hours to finish. Upon careful consideration, even the 1 s approach time is prohibitively long. A 250 x 250 pixel scan, which is common for our higher resolution images, includes 62,500 individual locations and would require over 17 hrs for completion. These issues could likely be addressed with modifications to the loop governing the approach but were instead bypassed with a different scanning strategy altogether.

The current scanning strategy does not attempt to accurately approach specific locations, but instead relies on accurate position reading of a close-to-target location. The discrete measurement locations are chosen according to the scan size and resolution as normal, and the piezo controllers are stepped through the locations using the naive voltage-to-position conversion as in the original approach. However, after setting the voltage for the target location, the true location is recorded from the strain gauge and stored along with the MIM data. The recorded positions are not necessarily spaced evenly. Later, the MIM and location data are passed to an interpolation function that performs a fit to the MIM data as a function of the X and Y coordinates. An evenly spaced set of positions spanning the measurement range with the same resolution of the scan is then passed to the interpolation function, which outputs the estimated MIM response at that position. This interpolated MIM signal at evenly spaced locations is much simpler to plot in MATLAB and with reasonably dense data sets, errors from plotting a fit vs raw data are negligible. Data are only recorded in the forward scan direction, and at the end of each scan line the piezo moves back to start the next line in a predefined number of steps (usually 50) without recording data.

This approach is limited only by the speed at which MATLAB can set the piezo voltage, the length of a short pause command included to let the piezo stabilize, and the time it takes to read the strain gauge and MIM data. The highest resolution we typically choose is 301 x 301

pixels, which takes roughly 2 hrs using this method, and low-resolution scans finish on the order of 10 mins.

Another issue we observed during testing on exposed single- and double-layer graphene flakes on hBN was the eventual destruction of the graphene with repeated scans. The relatively stiff RMN 25Pt300C cantilevers have even been seen to damage multilayer hBN if the contact force and scan rate are too high. The contact force between is determined by the spring constant of the AFM probe and the magnitude of the laser deflection prior to the tip touching the sample. This latter parameter is relatively easy to control when starting a scan as explained here.

The light that hits the photosensor after being deflected from the cantilever is not focused to a single point, and instead covers a large area of the sensor. The sensor is divided into equal quadrants, with the dividing lines parallel to the X and Y axes of the sample stage. The software quantifies the amount of light hitting each quadrant as a voltage and takes the difference between the sum of voltages on the right two quadrants and left two quadrants to determine a single value, called XDIFF. Similarly, the difference between the sum of voltages on the top two quadrants and the bottom two quadrants is called YDIFF. The XDIFF and YDIFF voltages are displayed by the AFM software along with a graphical representation of the photosensor (Figure 21). A small circle depicting the center of the laser is plotted on the graph using XDIFF and YDIFF as X and Y coordinates. The location of the circle aids with laser alignment but also determines the force applied upon contact. The long axis of the cantilever is parallel to the X axis, so when the tip touches the sample and the cantilever is bent upward, the laser deflects toward the right side of the graph and the XDIFF value increases while YDIFF remains relatively constant. To engage the tip with the sample and maintain good contact, the laser is adjusted so the XDIFF value is slightly negative and the YDIFF value is near zero. The Z-piezo begins fully extended, and then the sample stage is manually raised until the tip touches the sample, and the laser begins to deflect to the right and XDIFF begins to increase. Once

XDIFF reaches zero, manually raising the stage further results in the Z-piezo shrinking to maintain a zero XDIFF value and a constant contact force. During scanning, the Z-piezo actively responds to the laser deflection to maintain XDIFF at 0 V. So, the value of XDIFF prior to the tip touching the sample determines how far the stage must be raised to get XDIFF to zero and also how much the cantilever bends before the Z-piezo starts maintaining a constant force. The AFM manual recommends a starting XDIFF value of -0.1 V to ensure good contact during scanning, but this is the value that was used in early scans of graphene samples and was shown to cause damage.

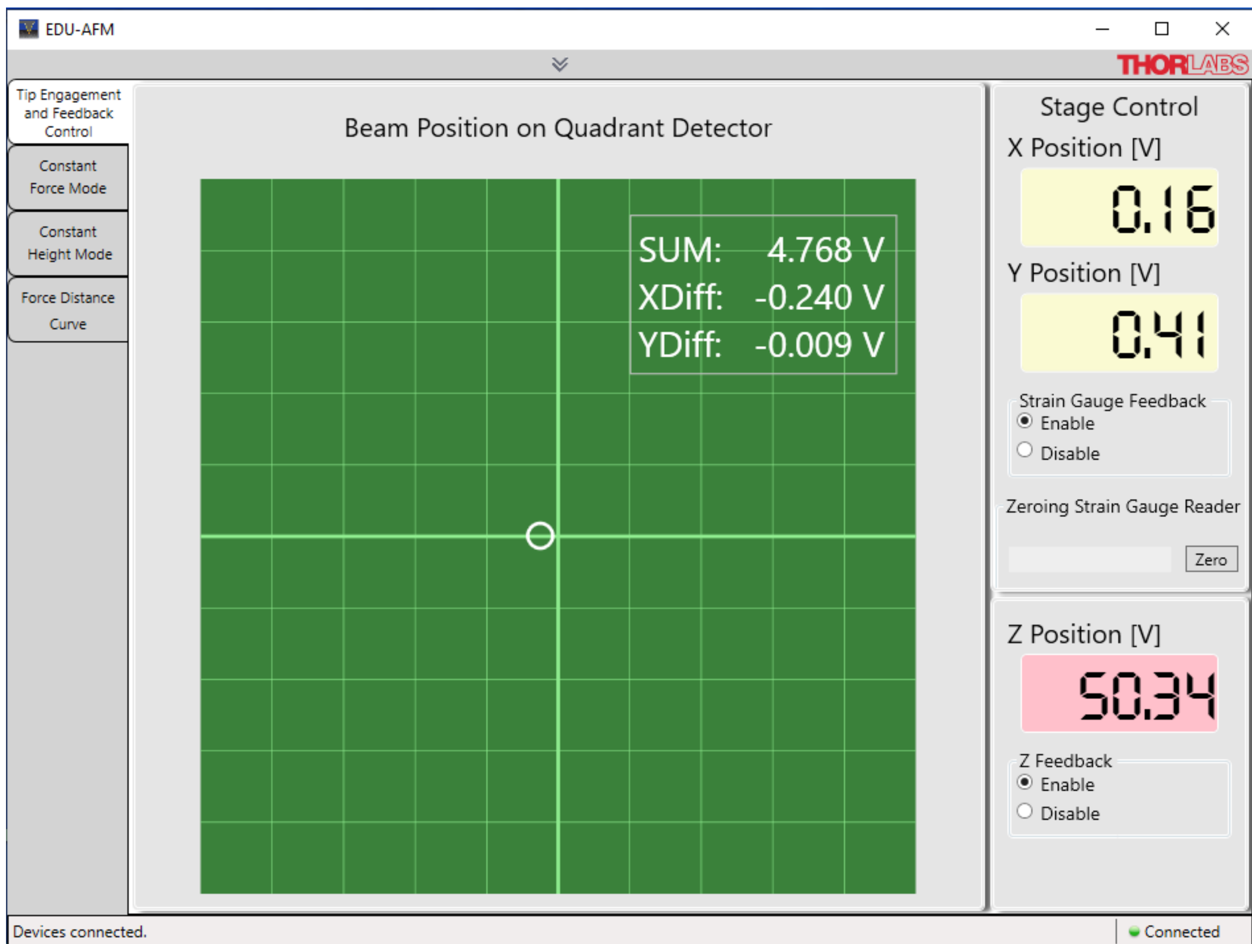

Figure 21: EDU-AFM1 software showing the grid representing the photosensor. The center of the laser is shown by the white circle with (X, Y) coordinates (XDIFF, YDIFF). The value of XDIFF before the tip makes contacts determines the relative force applied.

To explore safe starting values for XDIFF when using the RMN 25Pt300C probes, graphite was exfoliated on a Si/SiO2 wafer and monolayers were identified optically. AFM/MIM scans were performed using smaller starting XDIFF values to first locate a monolayer, and then MIM scans were iterated on one region of the monolayer to observe the effects of repeated scanning (Figure 22). No damage was observed after six repeated scans where the XDIFF value was between -0.035 V and -0.010 V before contact. The laser deflection was observed to drift with time, so it was necessary to check the uncontacted XDIFF value between each scan and sometimes adjustment was necessary to bring it back inside the -35 to -10 mV range. If XDIFF decreases too much, the risk of damage increases. If XDIFF increases too much it can pass zero and turn positive, which the software interprets as a tip crash. In response, the Z-piezo contracts fully and the tip loses contact with the sample. In principle, if the -35 to -10 mV XDIFF range is safe for a relatively fragile graphene monolayer, which this test appeared to indicate, then it should be safe for almost any other sample we would want to test. Probes with lower spring constants than 18 N/m should also be safe to use with this precaution.

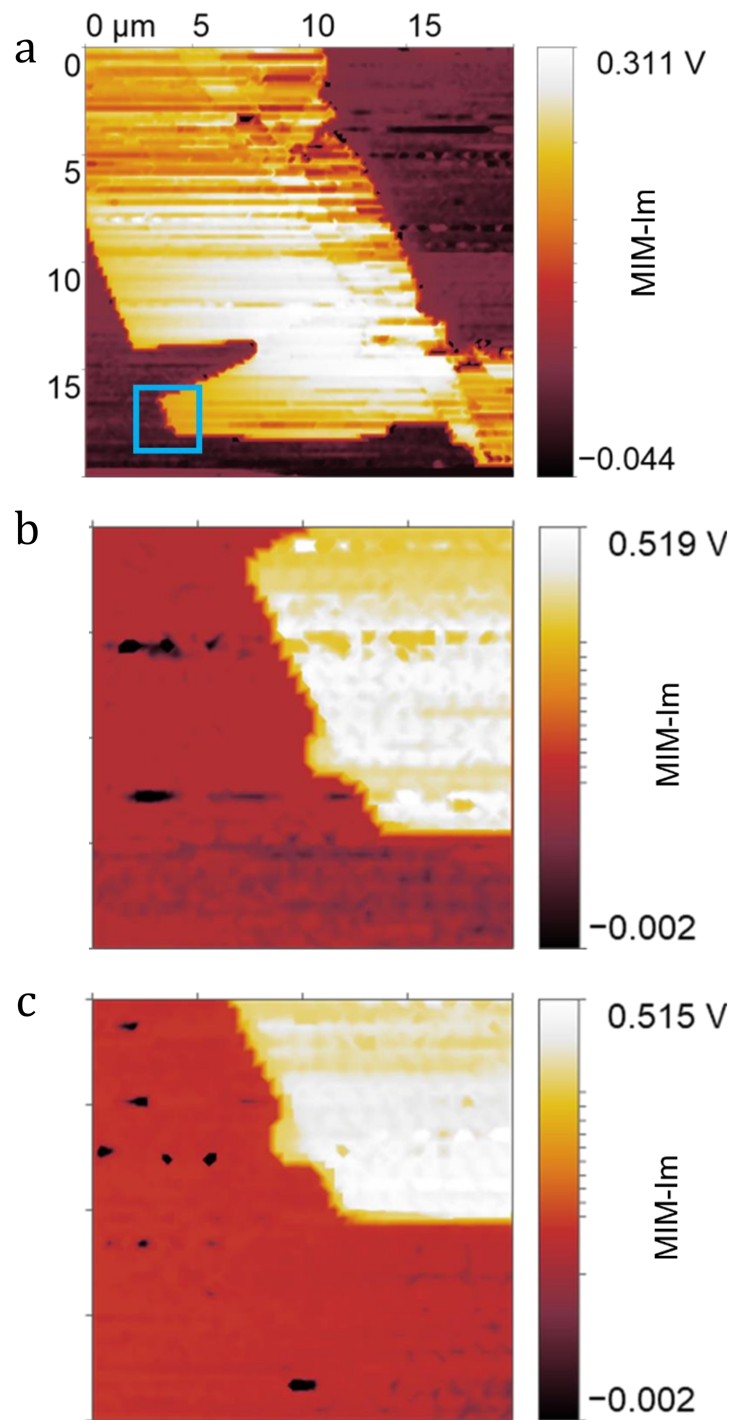

Figure 22: a) Wide area scan of a graphene flake with a small contact force. The blue rectangle marks the region covered by the small area scans. b) First small area scan, second scan overall. c) Fifth small area scan, sixth scan in total.

We have also demonstrated voltage modulated MIM, or dC/dV mode imaging, as described in section 1.3.2. To test this functionality, a scanning capacitance microscopy (SCM) test sample from Bruker was imaged with a 0.5 V_{rms}, 5kHz excitation added to the tip. The sample is a cleaved portion of a static random access memory chip without metallic or oxide capping layers, and the exposed Si structures have small p- and n-doped regions that are useful for SCM demonstrations (Figure 23), but also for MIM-dC/dV imaging (Figure 24) [14], [16].

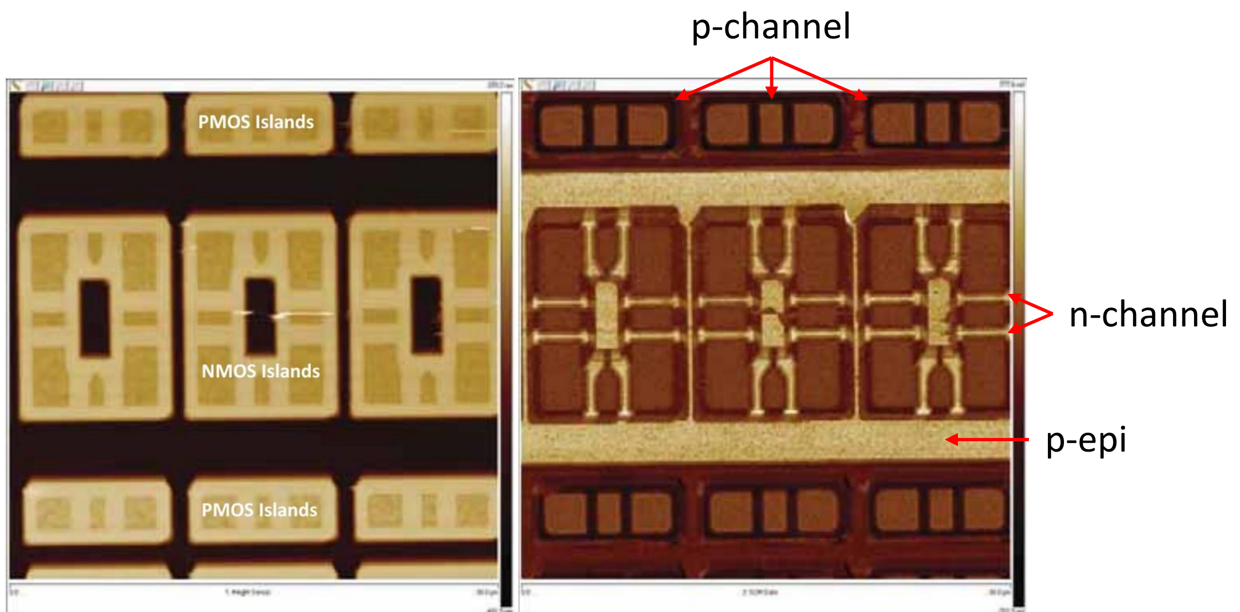

Figure 23: Bruker's AFM (left) and SCM (right) images of their SRAM sample [6].

In dC/dV mode, regions that are weakly p- or n-doped are relatively susceptible to electrostatic doping from the low frequency excitation on the tip. As charge carriers alternately accumulate and disperse under the tip, the tip-sample capacitance, and therefore the MIM response, changes dramatically. Strongly chemically doped regions are less susceptible to further doping from the tip voltage, and the MIM signal does not vary much with the low frequency voltage when the tip contacts these areas. Mapping the amplitude of the MIM-dC/dV response differentiates between weakly and strongly doped regions and mapping the relative phase of the response differentiates between weakly p- and weakly n-doped regions. Strongly

doped regions of both dopant varieties are difficult to differentiate in either the amplitude or phase maps.

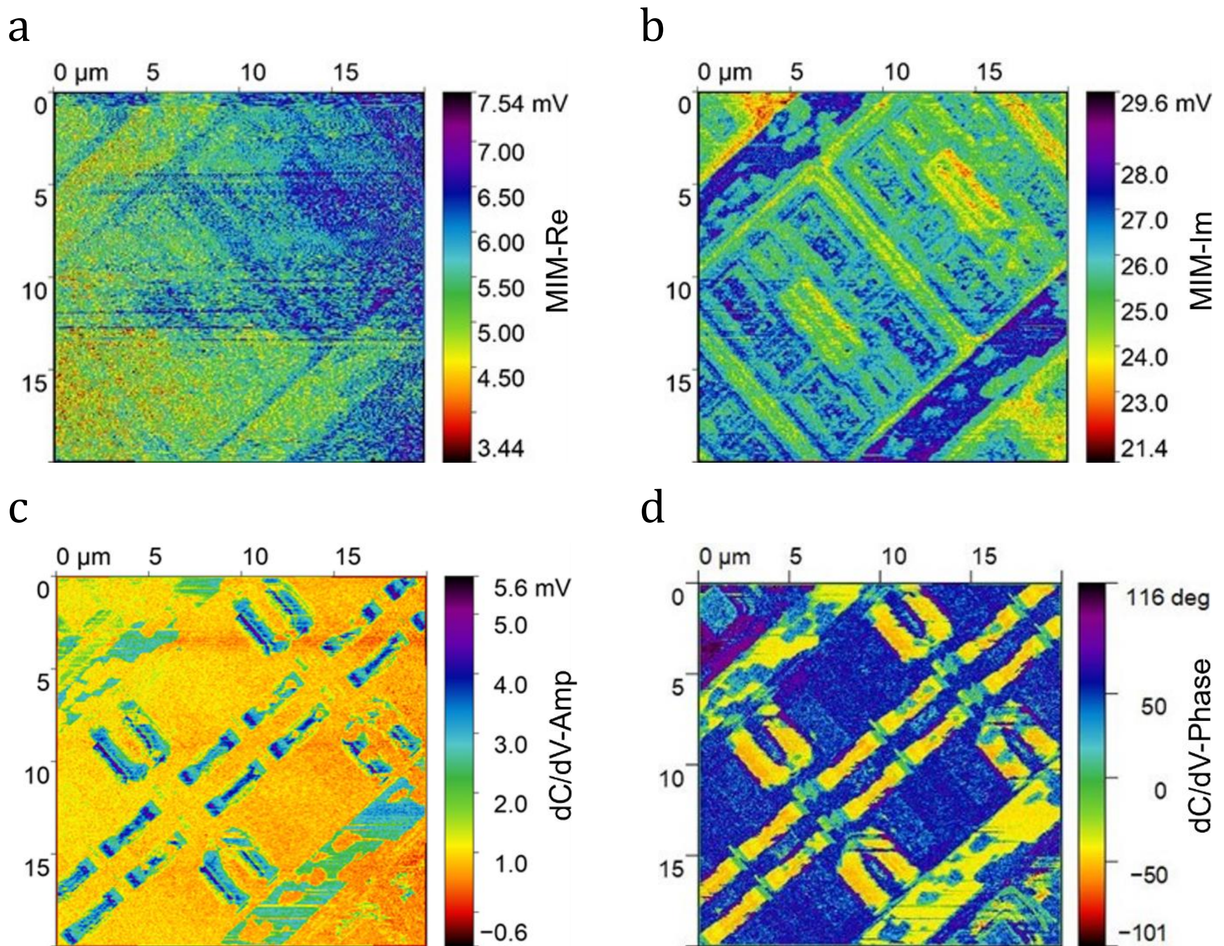

Figure 24: a) MIM-Re, b) MIM-Im, c) dC/dV-Amp, and d) dC/dV-Phase of the static random access memory sample from Bruker. The dC/dV-Amp signal (c) is largest in regions with minimal doping, while the dC/dV-Phase signal (d) helps distinguish between lightly n-doped regions (more purple) and lightly p-doped regions (more red).

Regular MIM images of the sample show a relatively weak MIM-Re response and a strong differentiation between regions of different conductivity (Figure 24). Additional distinctions are made clear in the dC/dV amplitude and phase images of the Bruker SRAM sample. The n-channel, p-channel, and p-epi regions show a strong response in the amplitude map because of their relatively weak dopant concentrations. Differentiating between the n-channel/p-epi regions and the p-channel is possible in the phase map, which is sensitive to the dopant types. The more strongly doped sample regions show little amplitude response, and a middling phase

response, as expected. Our phase map agrees well with the SCM image provided on Bruker's website (Figure 23).

This technique should be straightforward to apply to other doped semiconducting samples, and in principle can also distinguish between oppositely polarized domains in ferroelectrics, where the MIM-dC/dV response is dependent on the lowest order nonlinear dielectric constant, which in turn depends on the local polarization direction [13], [15].

2.5.4 WTe_2 Tests

We performed an MIM test on a WTe_2 flake contacted by Pd and encapsulated in hBN with a graphite back gate. The device had not been showing a connection to the Pd contacts in transport tests and the goal of the MIM tests was to corroborate this observation. By grounding all the contacts and sweeping the back gate voltage while keeping the MIM tip stationary on the sample, charge carriers should accumulate and deplete in the WTe_2 flake and the MIM signal should show a corresponding change. However, no clear change in the MIM signal was observed as a function of back gate voltage so we concluded that no Pd contacts were connected to the WTe_2 flake.

During the tests, two types of damage to the sample were also observed (Figure 25). In one location a hole was torn in the device due to improper attention to the XDIFF parameter prior to scanning. This damage is well understood as discussed in section 2.5.3. Additionally, several of the Pd contacts disappeared over the course of the tests. Optical images taken before the transport tests and after the MIM scans showed Pd contacts that were partially or completely missing. Initially we assumed the exposed Pd had not adhered well to the hBN and was scraped away by the MIM tip, but a more thorough investigation found similar damage in samples that had undergone transport tests without any AFM or MIM scanning. The missing Pd contacts were not akin to damage resulting from electrical shocks, which tend to blow up large

sections of the 2D flakes in addition to damaging metallic contacts. We have since stopped fabricating samples with exposed Pd contacts to avoid this issue completely.

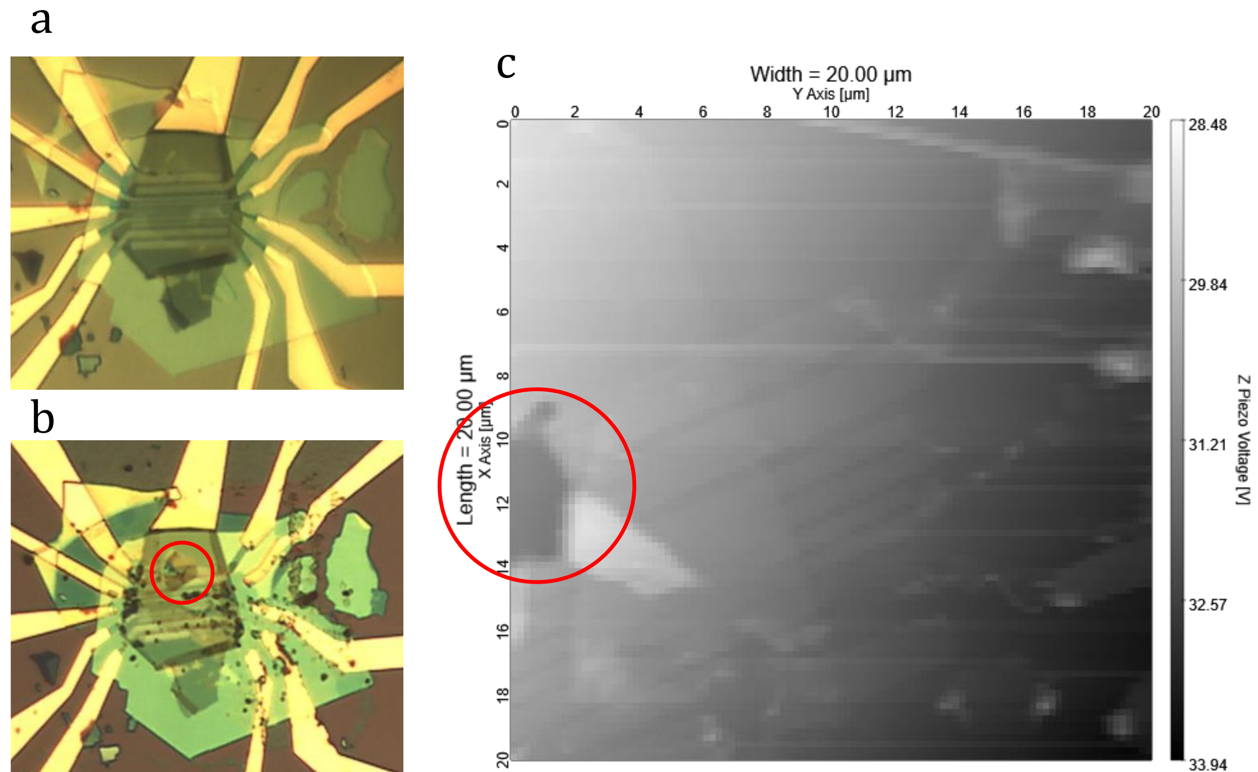

Figure 25: WTe_2 sample. a) Optical image taken before transport or AFM/MIM scanning. b) Optical image taken after transport and AFM/MIM scanning. The Pd contacts connecting the large gold electrodes to the sample are damaged and a small tear in the sample is visible in the red circle. c) AFM image taken after AFM/MIM scanning. The Pd contacts are damaged and the same tear is easily visible in the red circle.

2.5.5 Graphene on $RuCl_3$ Tests

One device made of graphene on $RuCl_3$ with a doped Si back gate was imaged with the goal of observing charge transfer due to a difference in work functions between the two materials [17], [18]. Six Cr/Au contacts were also deposited on the graphene for transport tests, but initial checks showed current leakage between the contacts and the back gate, and further transport tests were abandoned.

The AFM scans used to locate the sample avoided the sample center where the graphene was transferred to avoid accidental damage, but the first MIM images showed no graphene region at all. This was not consistent with flake damage from the tip, which is a

gradual process that occurs with successive scans. The complete lack of a graphene flake from the beginning instead pointed toward a problem in the fabrication process.

Additionally, some of the metallic contacts were bent by successive MIM scans. The relatively tall profile of the contacts (100 nm), the stiffness of the tip (18 N/m), the thickness of the adhesive Cr layer (5 nm), and the orientation of the contacts close to parallel with the fast scan direction likely all contributed to the deformation. Nearby contacts that were deposited in the same fabrication step but oriented at a larger angle relative to the fast scan direction were not affected.

A second graphene flake was transferred on top of the $RuCl_3$ in an attempt to salvage the sample. This second flake and the metallic contacts were visible in MIM scans (Figure 26). However, the graphene flake appeared fractured into several sections, and device areas where graphene overlapped with $RuCl_3$ did not show distinct differences compared to graphene-only regions. The fracturing of the flake most likely resulted from the transfer process and not tip

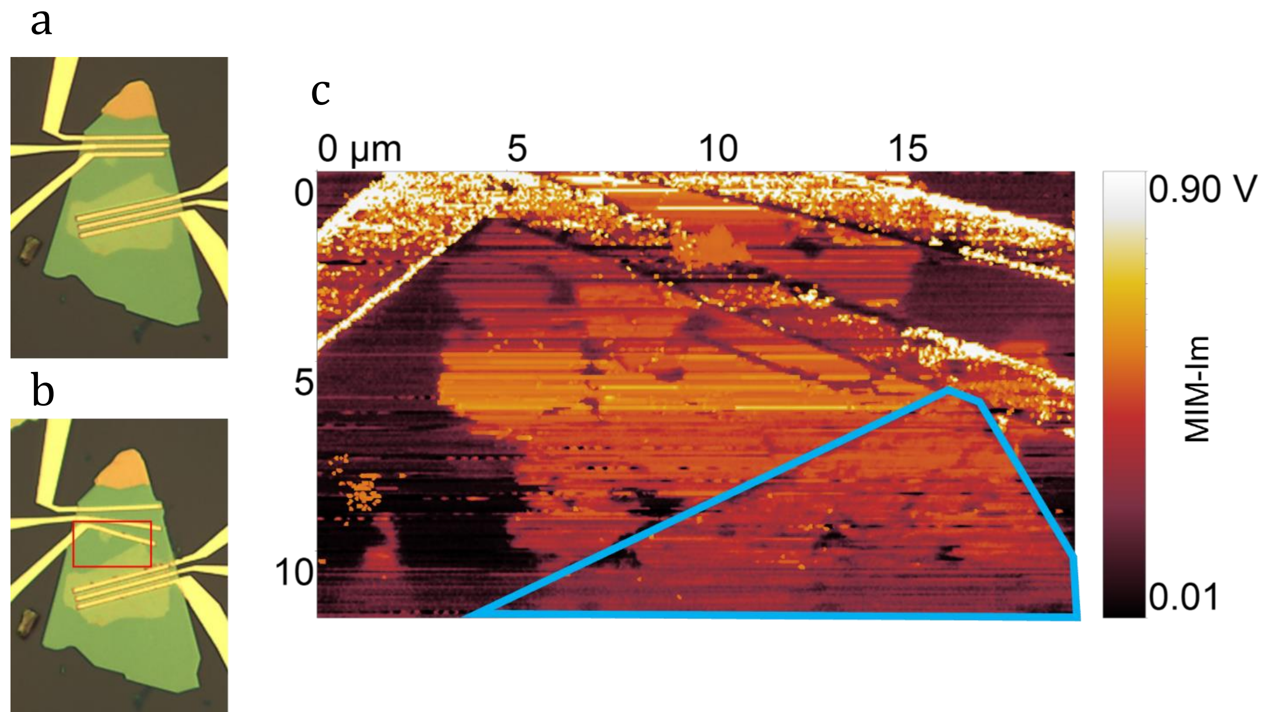

Figure 26: $RuCl_3$ sample. a) Optical image taken before AFM/MIM scanning. b) Optical image taken after AFM/MIM scanning with the area scanned in (c) outlined by a red rectangle. c) MIM scan of the sample showing the second graphene flake in orange. The graphene flake is fractured into several sections and the region covering the $RuCl_3$ (outlined in blue) does not show any distinct differences.

damage, because the fractures do not align with the scan direction. Additional tests are needed to determine whether useful physical results could still be obtained from a graphene/$RuCl_3$ stack, ideally with samples that do not show current leakage so transport tests and additional MIM pictures at several back gate voltages could also be acquired.

2.5.6 Nano3 Tests

Additional tests were performed by incorporating our MHz MIM circuit with the Veeco SPM in the Nano3 user facility on campus. We received permission to reserve a full day on the equipment and modify it for MIM imaging to compare its performance with our tabletop AFM and to try imaging ferroelectric domains in parallel-stacked bilayer hBN [19], [20].

Initial imaging was performed on the Bruker SRAM sample to confirm the performance of the regular MIM and dC/dV methods (Figure 27). Steps to significantly reduce the noise were required to successfully calibrate the cancellation signal, including turning the electronics rack away from the user and blocking the front of the electronics rack with a tall acrylic pane covered in aluminum foil. The acrylic pane was formerly used by the facility for social distancing purposes and was large enough to shield most of the electronics. Subsequent MIM images of the encapsulated graphene sample demonstrated that the Veeco system was unlikely to damage 2D samples when using 12PtIr400C probes. The regular MIM images showed increased noise levels and the Veeco control software does not allow the tip to contact the sample and remain stationary, so the reference phase could not be calibrated and the MIM-Re and MIM-Im channels were arbitrarily mixed. Instead of MIM-Re and MIM-Im the data from the Nano3 tests are labeled channel 1 (Ch1) and channel 2 (Ch2) to avoid confusion.

Tests of two hBN stacks did show evidence of ferroelectric domains in dC/dV mode. Neither regular MIM nor dC/dV imaging clearly resolved a difference between the hBN and the SiO2 substrate, making it difficult to draw conclusions about the setup’s capacity to image ferroelectric domains. Because both materials are insulating, the only contrast expected in

regular MIM imaging would come from a difference in dielectric constant between the materials. Contrast has been resolved between thick hBN and SiO2 in the past (e.g. the encapsulated graphene sample), but the contrast difference would be much smaller for very thin hBN. The lack of ferroelectric domains in the dC/dV images could be a result of improper implementation of the technique for ferroelectric domains, which may require subtle differences in the approach as compared to dC/dV imaging on doped semiconductors. Additionally, the lack of ferroelectric domains stem from a fault in the sample fabrication process, of which these two samples were the first products. More tests would be useful in determining if one or both possibilities are affecting results and how best to address them.

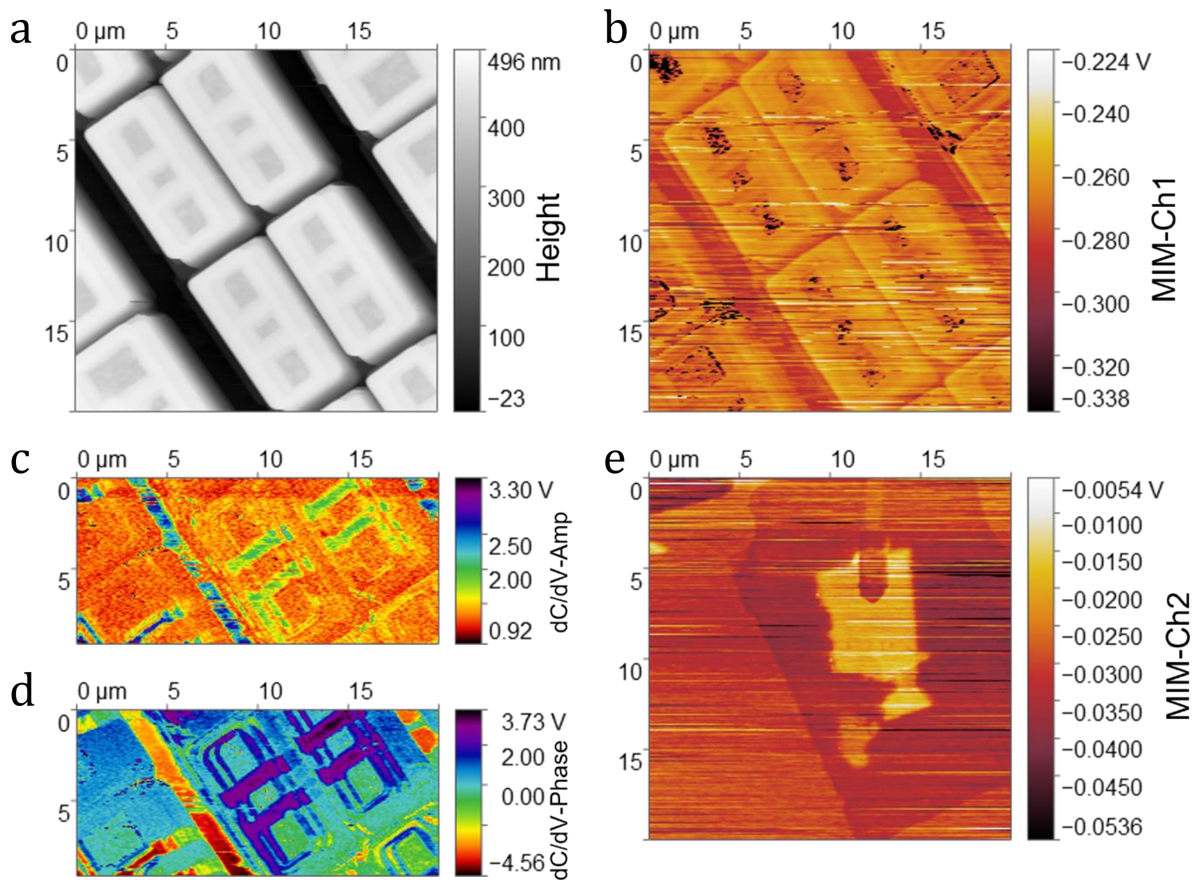

Figure 27: Data from the first tests using the MHz circuit in Nano3. a) AFM image of the SRAM sample. b) MIM-Ch1 image of the SRAM sample. c) dC/dV-Amp image of the SRAM sample. d) dC/dV-Phase image of the SRAM sample. e) MIM-Ch2 image of the encapsulated graphene sample.

A second day of tests in Nano3 focused on imaging exposed graphene on hBN, in the hope of observing a Moiré pattern resulting from the mismatch between the graphene and hBN lattices. Significant signal noise continued to pose a problem and image quality appeared to degrade as the scan area was reduced. No images showed a Moiré pattern but additional trials are needed to conclude whether these challenges can be resolved or if imaging Moiré patterns is not a viable goal with this system.

2.6 2-10 GHz Circuit

2.6.1 Development

The 2-10 GHz circuit, like the 1 GHz circuit, is based on a design from the Shen group at Stanford (Figure 28, Figure A.5). It has the widest operating range of the three circuits and is useful for particularly conductive samples. It was constructed soon after the completion of the MHz circuit and tested immediately after. Many of the software problems were addressed while testing the MHz circuit, and the assembly of this circuit benefited from the experience of assembling and troubleshooting the other two circuits, so imaging with the 2-10 GHz circuit worked almost immediately after integrating it with our AFM.

The 2-10 GHz circuit, like the 1 GHz circuit, requires a separate power supply, a dedicated microwave source, two voltage pre-amplifiers, and DC voltage sources and readout (Figure A.6). This last need is satisfied by an SR830 lock-in amplifier which has four analog inputs and outputs, and its lock-in functionality is useful for dC/dV imaging.

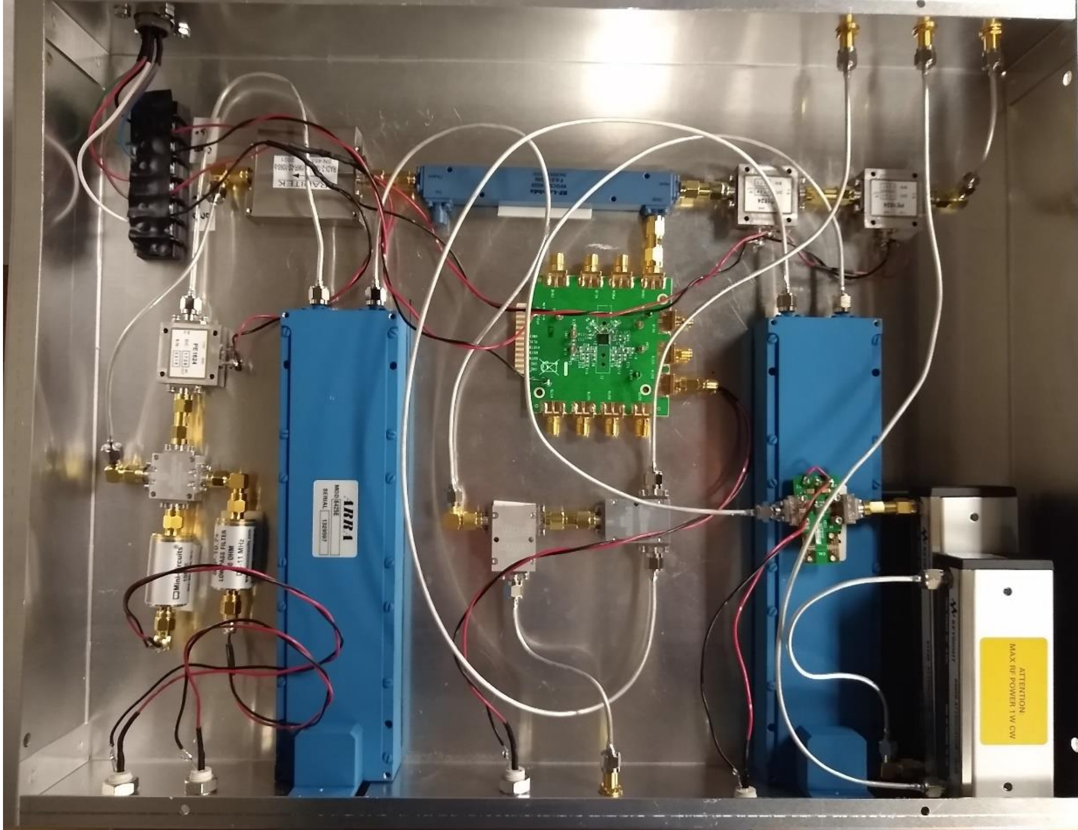

Figure 28: Image of the 2-10 GHz MIM circuit

2.6.2 Initial Testing

Testing of the 2-10 GHz circuit began after the MHz tests concluded. Switching between the two only required changing the MHz IMN out for a λ/2 style IMN with acceptable resonances. Testing began with the Al squares sample mentioned previously and good contrast between the Al and SiO2 was obtained with little difficulty (Figure 29). Tests then progressed to an exposed graphene sample on hBN to observe a Moiré pattern. After the MHz tests failed to resolve a Moiré pattern, we hoped that a higher frequency measurement would provide better contrast. No Moiré pattern was observed, and damage of the flake with successive scans was seen again as in the MHz case. This concluded the tests of the 2-10 GHz circuit and the Leiden dilution refrigerator with the custom Attocube SPM attachment arrived shortly after. Since then,

the 2-10 GHz circuit has been dedicated to that system and Rajarshi Bhattacharyya and Leonard Cao have demonstrated cryogenic imaging of several test samples.

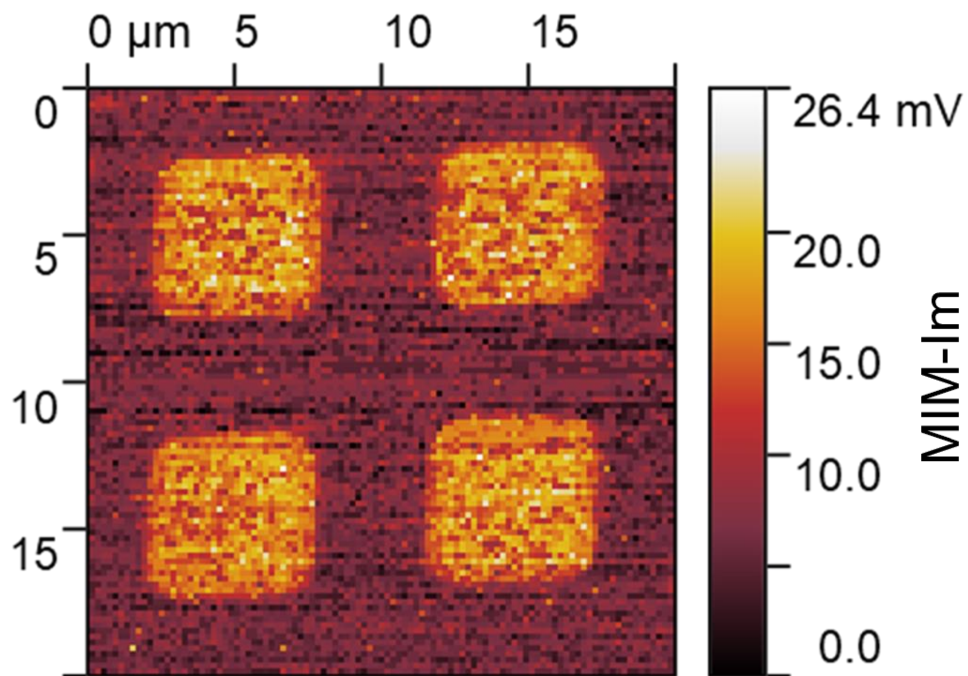

Figure 29: MIM-Im image of the Al squares recorded using the 2-10 GHz box

Chapter 2 is coauthored with Allen, Monica. The thesis author was the primary author of this chapter.

3 Conclusion

This thesis has presented the development of our room temperature microwave impedance microscope. Challenges in creating a working setup and their solutions have been discussed along with current obstacles and possible fixes. Here I outline ideas for future studies using the room temperature MIM.

In the near future, tests comparing the performance of RMN's 12PtIr400C probes to the 25Pt300C model would be helpful. Our hope is that the 12PtIr400C probes will be much more forgiving in contact mode scans on our thin flake samples. While the reduced force scanning method described previously has largely prevented flake damage when using the tabletop AFM, drift in the XDIFF value is a constant concern and without careful adjustment between scans it is easy to accidentally apply too much force. The lower spring constant of the newer 12PtIr400C model could eliminate the need to monitor XDIFF entirely.

Simulations in COMSOL Multiphysics of the expected MIM response on 2D samples with anisotropic electrical conductivity predict unusual edge modes in the MIM-Re signal. Simulations on square flakes with anisotropies taken from studies black-As [21] and GaTe [22] both show edge signals that appear to shift between the horizontal and vertical flake edges as a function of frequency (Figure 30). Simulations of the MIM-Im response do not show notable behavior, and the fundamental cause of the MIM-Re edge signals is still unknown. The basic theory of MIM does not consider anisotropic conductivities or predict any response. Confirming the existence of these edge signals in a real sample would indicate that the current theory of MIM is incomplete. If these edge signals appear in a material like black-As or GaTe, which show anisotropy along orthogonal crystal axes, it would be interesting to broaden the scope of tests to include materials like ReS2 which exhibits electrical anisotropy along non-orthogonal axes [23], [24]. If the response is related to the angle between the relevant axes, MIM could serve as a unique probe of electrical anisotropy that doesn't require patterning many contacts along the

radii of a circle as is the current approach. Recent studies on the effects of stacking order on hBN and transition metalichalcogenide bilayers have shown Moiré patterns of out-of-plane ferroelectric domains [19], [20], [25], [26]. Simultaneous MIM and dC/dV measurements could visualize spatial variations in conductivity, dielectric constant, and polarization to provide additional insight into these systems.

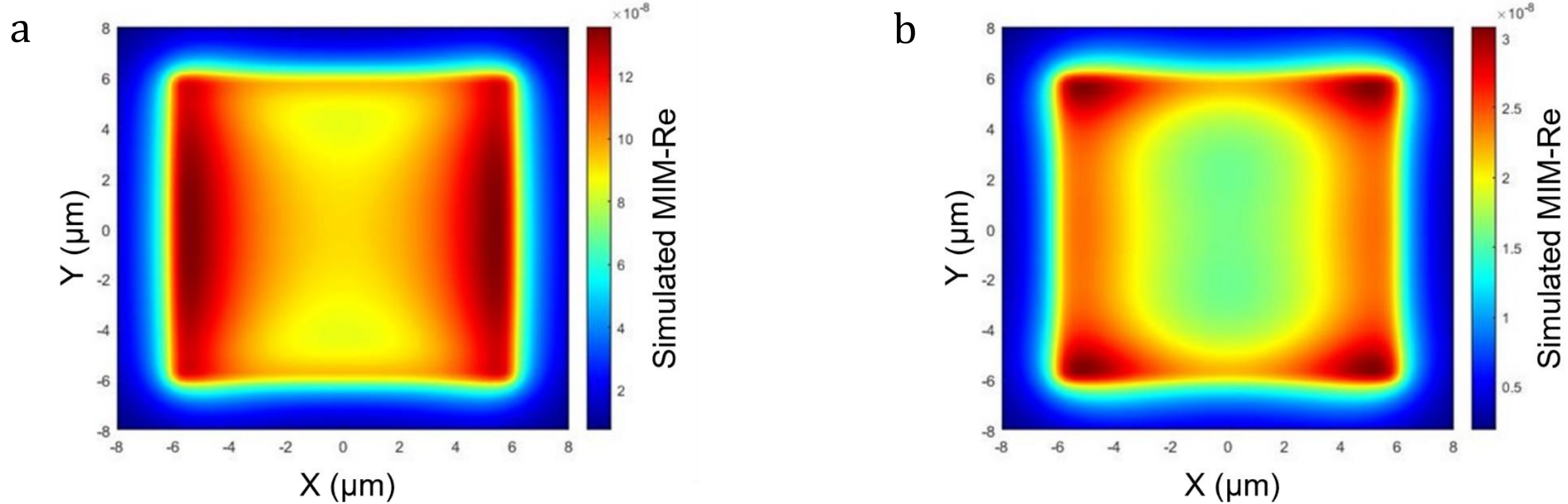

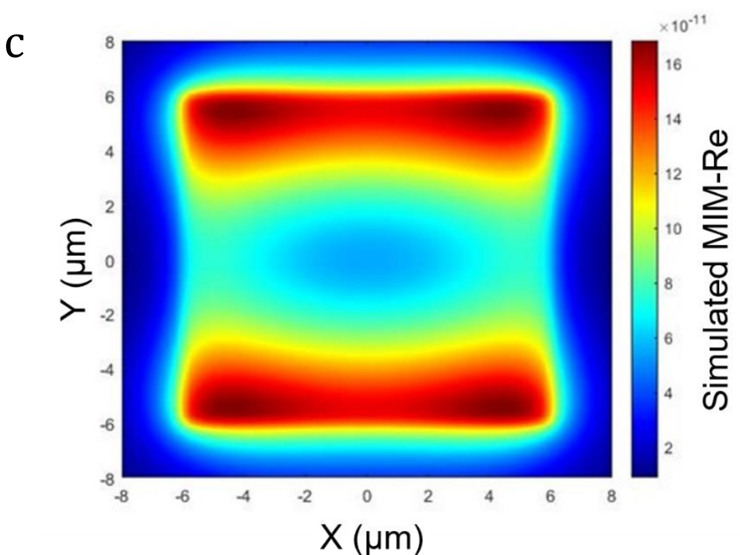

Figure 30: Spatial maps of the MIM-Re signal on a black-As sample simulated by COMSOL at a) 150 MHz, b) 3 GHz, and d) 10 GHz. Lateral scale is in µm.

Appendix A Circuit Diagrams

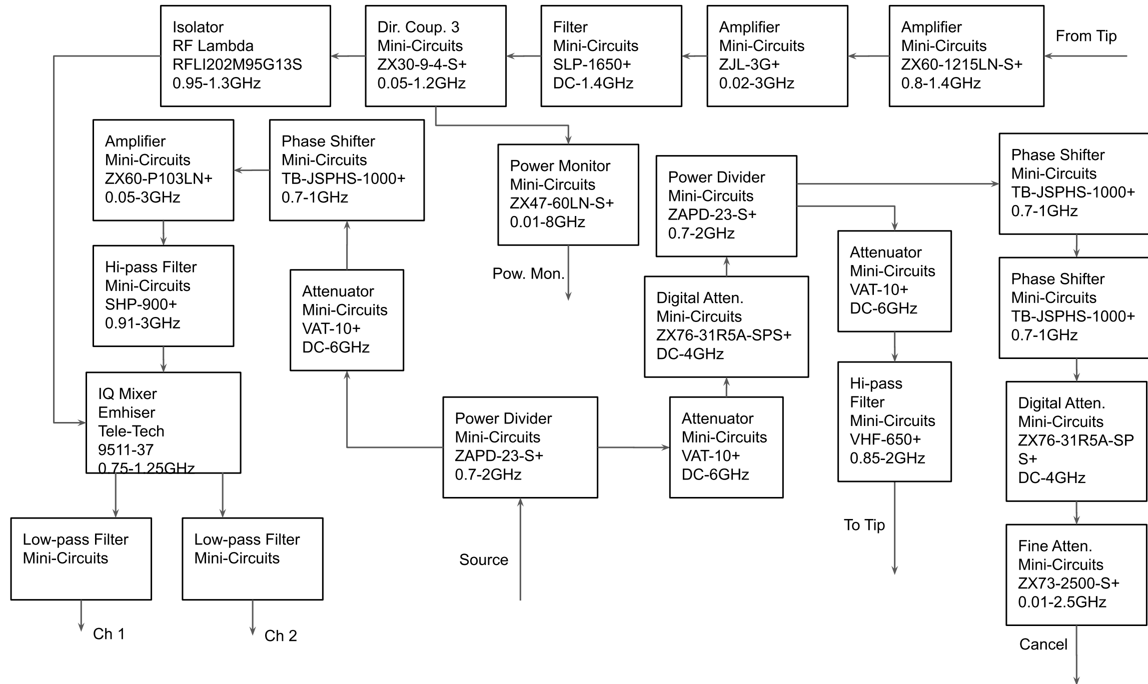

Figure A.1: Circuit components inside the 1 GHz MIM box

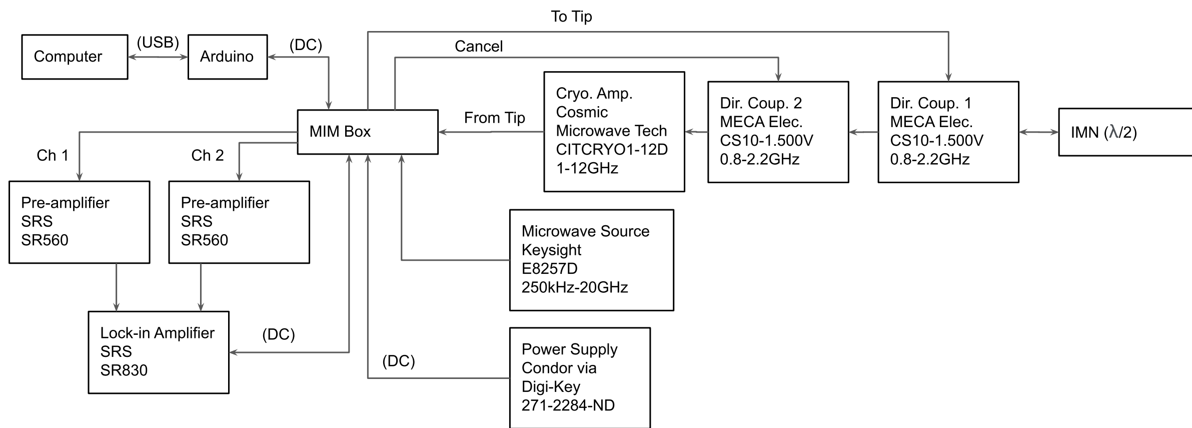

Figure A.2: Circuit components outside the 1 GHz MIM box

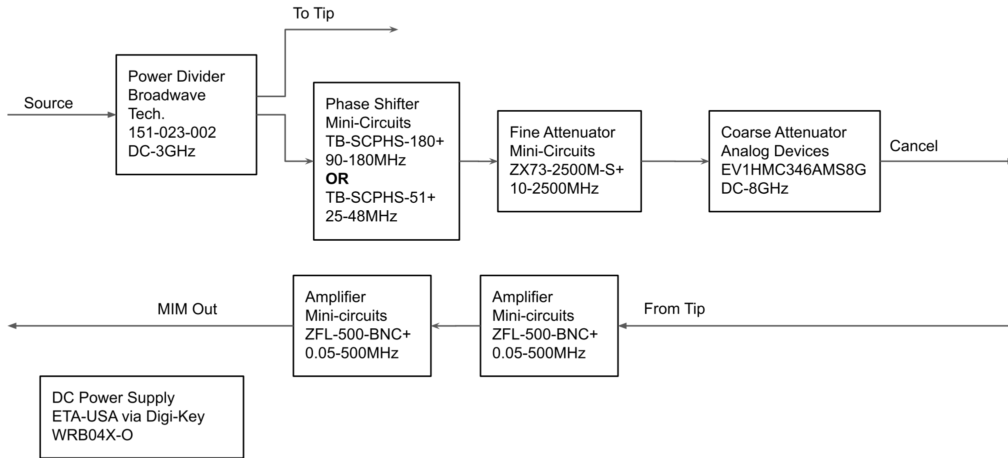

Figure A.3: Circuit components inside the MHz box

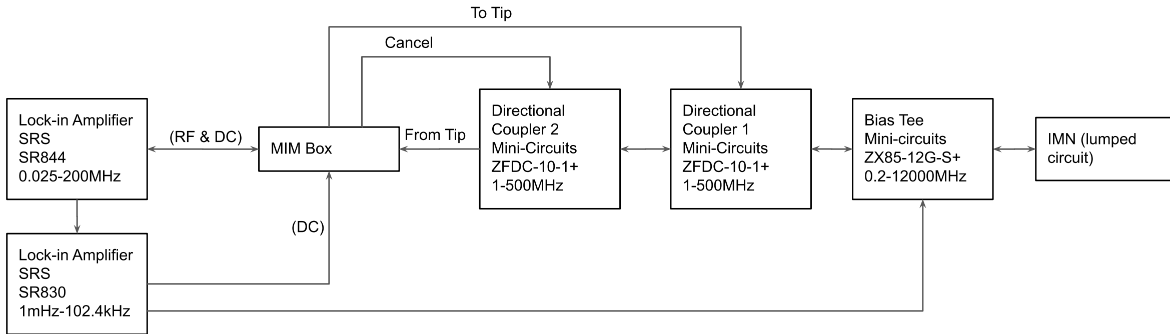

Figure A.4: Circuit components outside the MHz box, including the bias tee for dC/dV measurements

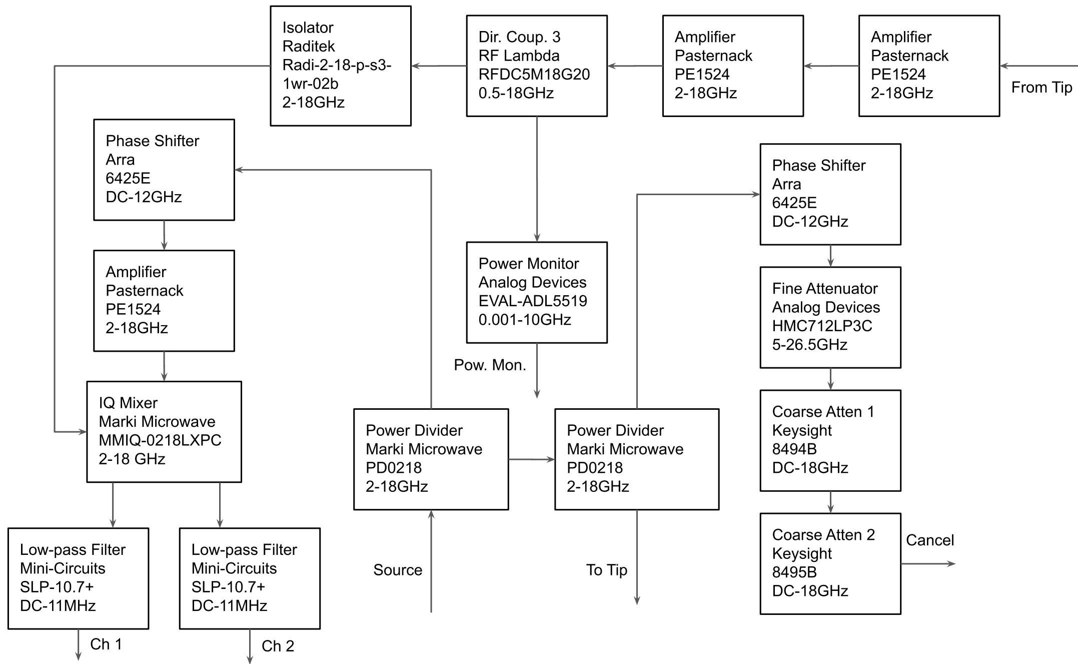

Figure A.5: Circuit components inside the 2-10 GHz box

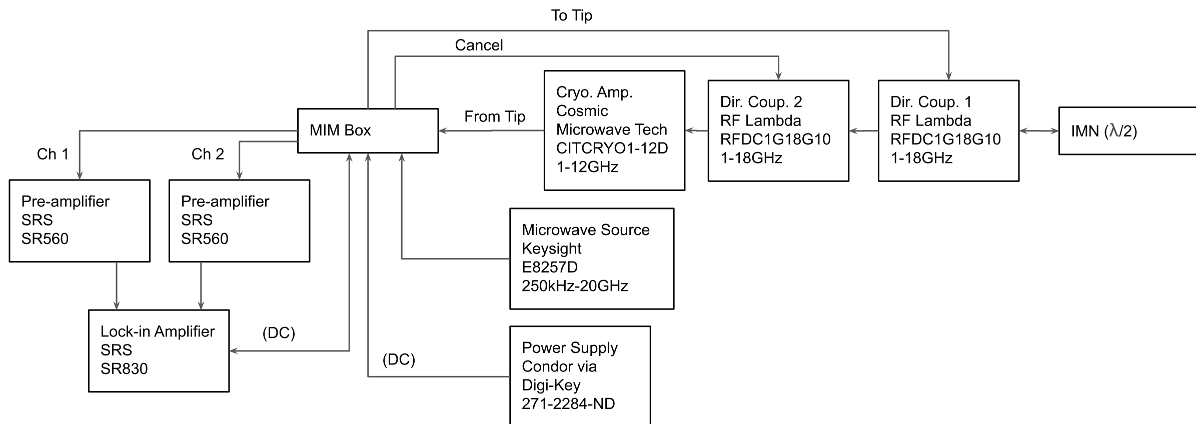

Figure A.6: Circuit components outside the 2-10 GHz box

Appendix B Common Issues and Fixes

B.1 1 GHz MIM Circuit

Problem: The digital attenuators are not responding to commands properly.

Solution: Ensure that the relevant attenuator variable is properly defined and the other attenuator variable is cleared before the command to change the attenuation value is sent. Make sure the bitrate is sufficiently small (25,000 bits/s). Read the Attenuation_v3.m annotations for additional details.

Problem: The Arduino became disconnected.

Solution: Reconnect the colored wires according to the following correspondence. Red – 45, White – 47, Brown – 51, Green – 52, Blue & Black – GND

Problem: The power supply will not turn on.

Solution: Check the fuse and replace if necessary. The fuse will blow if the power supply is turned on within 1 minute of being turned off.

B.2 MHz MIM Circuit

Problem: The dip in the coarse attenuator is near the end of its range. This may also be characterized by a noisy MIM signal and/or the dip in the fine attenuator being far from the starting value of ~8V. This often happens when probes and/or IMNs are switched out and the matching becomes better/worse.

Solution: If the dip in the coarse attenuator is near or beyond the low end of the range (-4V) then the ideal attenuation value is lower than achievable. Remove a passive attenuator (Mini-

Circuits VAT-10+) from the Cancel port on the MIM box, or add one to the To Tip port. If the dip is near or beyond the high end of the range (0V) then the ideal attenuation is higher than achievable. Remove a passive attenuator (Mini-Circuits VAT-10+) from the To Tip port or add one to the Cancel port.

Problem: The signal is generally noisy.

Solution: This could be a result of many issues. The cancellation calibration may be poor (the total power read by the SR844 should be <-30dBm before the tip contacts the sample). Ensure the gold wire is well-soldered to the IMN. Sit farther from the setup and use a remote desktop service (like TeamViewer) to control the setup while making sure no one else is nearby. Ensure all the SMA connections external to the MIM box are secure. The bias tee can make the signal noisier so consider removing it if you are not performing dC/dV measurements. Try increasing the resolution or adjusting the scan speed. Adding a metallic shield, like a cardboard box covered in aluminum foil, can sometimes improve the noise but placing anything near the setup also changes the cancellation calibration so recalibration is needed any time the shield is moved. This can be especially cumbersome if the shield needs to be moved every time the XDIFF value needs to be readjusted.

Problem: Samples are being damaged.

Solution: Refer to the discussion of the XDIFF parameter (section 2.5.3) to reduce the force applied by the tip and/or use a more flexible probe.

Problem: MATLAB crashes when the piezo/strain gauge GUI is opened.

Solution: Turn the K-Cube bank off and back on then restart MATLAB and try again. The computer may also need to be restarted.

Problem: The blogging code is running very slowly (sometimes >20 mins).

Solution: This can be an issue with large data sets. If the scan resolution is much higher than 100x100 pixels, expect a significant delay.

Problem: A horizontal portion of the scan is missing.

Solution: The laser probably drifted so XDIFF became positive, causing the Z-piezo to shrink completely and the tip to lose contact. The XDIFF value always drifts with time, especially if the laser has been turned off recently. Make sure XDIFF is in the right range and not too close to 0 V before starting the scan, considering the fragility of the sample and the flexibility of the probe.

B.3 2-10 GHz MIM Circuit

Problem: Sweeping the cancellation phase does not show a peak in the power monitor when the source frequency is lower than about 3 GHz.

Solution: Add/Remove SMA connectors/adapters and/or swap out the flexible SMA cable connecting the Cancel port to directional coupler 2. By altering the path length, the peak can be shifted into the accessible window. The phase shifter can shift the incoming signal by 90°/GHz so this should only be a problem at lower frequencies where the phase shifter is less effective.

Appendix C Notes on the Cryogenic Amplifier from my Visit to Cosmic Microwave Technology on 4/16/21

- The amp begins saturating above -45dBm rf power. It will definitely break at +15dBm applied rf power (see document appended at the end). In general the DC voltages they specify at 300K and 12K are sufficient to get the right gain.
- Supplying the gate voltages (Vg1, Vg2) with AA batteries is fine because very, very little current is drawn but supplying the drain voltage (Vd) with AA batteries will kill them quickly and you won't get reliable behavior from the amp
    - Do not just connect a resistor with a calculated value in series with the amp to apply the correct voltage because the effective resistance of the amp changes and you can destroy it this way
- The drain current (Id) is very sensitive to the gate voltages so small variations in Vg1 and Vg2 can reduce the performance
- Do not use relay switches or anything that can suddenly apply rf power to the amp because the sudden change in impedance can lead to destructive current/charge buildup
- The amp is generally pretty robust to applied DC voltages
    - There are internal voltage dividers that actually reduce the gate voltages further (just helpful to know but not practically useful for us)
    - It could *probably* take up to plus or minus 5V on the gate pins but they never need to go that high

- The drain pin is less protected and the amp WILL be destroyed if a negative voltage is applied to the drain pin (the bias regulator prevents this)

- They have seen problems in the past where a Dewar was not properly grounded and it picked up an AC voltage, this can damage the amp
- CMT used a custom voltage supply with current readouts and used a Keithley to read Id
- They test the amps with a calibrated noise source and the signal gets sent to a Noise Figure Meter
    - This tells them the gain and the noise coming from the amp
- There are three internal stages in the amplifier
    - The ideal Id at room temp is ~45mA (~15mA per stage)
    - The ideal Id at 12K is ~15mA (~5mA per stage)
- Vg1 controls the first stage, Vg2 controls the second and third stages
- When finding the right voltages at room temperature, they begin with Vd = 1.8V and Vg1=Vg2=~-3.5V. The low gate voltages prevent any signal getting through and the amp is basically off
    - Then they increase Vg1 until they get about 15mA of Id (from the first stage)
    - Then they increase Vg2 until they get about 45mA of Id (second and third stages)
    - Then they tweak Vg1 to minimize the noise without respect to how the gain is affected.
    - Then they tweak Vg2 to maximize the gain. There is a relatively narrow peak in Vg2 where the gain is best so small variations in Vg2 can lead to poor gain
    - Essentially, Vg1 primarily affects the noise level and Vg2 primarily affects the gain
- At cryo temperatures, the values all change and Vd should be closer to 1.2V

- At any temperature you can also try reducing Vd a little which can improve the noise somewhat but you then need to adjust the gate voltages according to the above procedure. This is something they are experimenting with themselves
- When the amp is cold, the long, thin wires running to the Vd pin have a non-negligible resistance so the voltage at the Vd pin is not the same as the voltage applied by the source. They use a second pair of wires to measure the voltage right at the Vd pin to get an accurate value for Vd (kind of like a 4-lead measurement). Otherwise the voltage applied to Vd can be too small and you won't get the right performance.
    - In principle you could measure the value you need to output at the source to get the desired Vd with a multimeter before cooling down, then just leave the source voltage at that value, but it's better to actively monitor Vd
- Often their amps can be tuned up to +40dB of gain by increasing Vg2 a little. They always provide voltage values that achieve +35dB gain (by tuning Vg2 down a little) because that is their guaranteed specification and that way if you need to match the gain of two amplifiers there is a little flexibility up and down
- Regarding the bias regulator
    - The power cable has monitor pins that show the voltages being applied to the pins. We could build something (e.g. with an Arduino) that reads these voltages in real-time and displays them on a computer for ease of use
    - However there are also terminals that allow for checking with a multimeter so this isn't critical
    - If you use a multimeter to check the voltage on the Id terminal, multiply that value by 100 to convert from voltage to current in mA (e.g. 0.491V on the Id terminal means 49.1mA of current is going through the drain pin). Do not check the Id

terminal with the multimeter in current mode because the result won't make sense and you may damage something

    - The bias regulator receives +5V and -5V as input and the outputs can be changed by turning the small screws with a trimmer tool.
    - The bias regulator is built so that it cannot supply voltages that would damage the amp

- If Vd is tuned before connecting the pins to the amplifier, you will likely need to tune it a little more to get it back to the right value afterward.
- If we decide to try a 77K setup, the biases needed will be very close to those specified at 12K
- Regarding thermal anchoring
    - They use #4-40 screws to attach a machined block of oxygen free copper onto the amp and then attach the block to something else. Some of their blocks are nickel-plated to reduce oxidation and others are gold-plated to both reduce oxidation and to provide better thermal conduction than the nickel. They gave us a gold-plated block for free and they are happy to provide a drawing of these blocks if we want to machine our own
    - They bolt their amplifiers directly to a 12K plate with the block mentioned above, and then connect it directly to the other components with as few connectors/cables as possible to reduce reflections.
    - The other components are not mounted to the plate but are thermally anchored with 2mil thick copper foil (attached via washers and screws) that is attached to the 12K plate (via washers and screws). This prevents strain that would otherwise be applied to multiple components fixed in place
    - They put indium foil in between the two surfaces that are joined by screw connections because it is soft and fills in the gaps and has good thermal

conduction. They provided us with a sheet of indium foil and they said it can be purchased from Indium Corporation but Steve likes to find it more cheaply on Ebay. I believe Monica's setup at Stanford used Indium between thermal interfaces too.

  - The 12K plate they screw the components into is gold-plated copper but they use stainless steel press-in nuts from McMaster-Carr for the hole threads because if the threads were cut from copper they would wear out too quickly
  - They also sometimes use oxygen-free copper wire twisted together and connected to a crimping ring terminal or soldered to more copper to create thermal straps. They buy old wire for speakers (which is apparently made of relatively high quality, oxygen-free copper) online, strip the insulation, and twist it together.
  - They pointed out that our network analyzer has built-in attenuators for both test ports that can be used to control their output power separately. Go to Menu → Attenuation Port ½

- See pictures below for additional details.

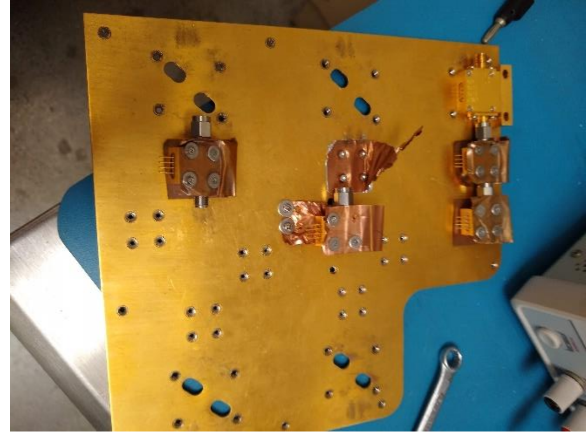

Figure C.1: Left: Their 12K plate. The components here are mechanically and thermally anchored with copper foil, held in place with washers and screws with a layer of indium foil for improved thermal contact. You can see the threads in the plate are stainless steel, press-in washers. Right: Another picture of their 12K plate, with the cryogenic amplifier included in the top right. It is anchored with a gold-plated copper block and screws.

Figure C.2: Left: Picture of the packaging of the copper foil they use. Top: A homemade thermal strap soldered at one end and crimped to a ring terminal at the other. The twisted copper threads are from old speaker wire. Bottom: Close up of the crimping ring terminal they use.

References

[1] Y.-T. Cui and E. Yue Ma, "Microwave Impedance Microscopy," in *Capacitance Spectroscopy of Semiconductors (1st ed.)*, Pan Stanford Publishing Pte. Ltd., 2018.

[2] D. Wu, A. J. Pak, Y. Liu, Y. Zhou, X. Wu, Y. Zhu, M. Lin, Y. Han, Y. Ren, H. Peng, Y.-H. Tsai, G. S. Hwang and K. Lai, "Thickness-Dependent Dielectric Constant of Few-Layer In2Se3 Nanoflakes," *Nano Letters,* vol. 15, pp. 8136-8140, 2015.

[3] M. E. Barber, E. Y. Ma and Z.-X. Shen, "Microwave impedance microscopy and its application to quantum materials," *Nature Reviews Physics,* vol. 4, pp. 61-74, 2022.

[4] K. Lai, M. Nakamura, W. Kundhikanjana, M. Kawasaki, Y. Tokura, M. A. Kelly and Z.-X. Shen, "Mesoscopic Percolating Resistance Network in a Strained Manganite Thin Film," *Science,* vol. 329, no. 5988, pp. 190-193, 2010.

[5] E. Y. Ma, Y.-T. Cui, K. Ueda, S. Tang, K. Chen, N. Tamura, P. M. Wu, J. Fujioka, Y. Tokura and Z.-X. Shen, "Mobile metallic domain walls in an all-in-all-out magnetic insulator," *Science,* vol. 350, no. 6260, pp. 538-541, 2015.

[6] E. Y. Ma, B. Bryant, Y. Tokunaga, G. Aeppli, Y. Tokura and Z.-X. Shen, "Charge-order domain walls with enhanced conductivity in a layered manganite," *Nature Communications,* vol. 6, p. 7595, 2015.

[7] Z. Chu, E. C. Regan, X. Ma, D. Wang, Z. Xu, M. Iqbal Bakti Utama, K. Yumigeta, M. Blei, K. Watanabe, T. Taniguchi, S. Tongay, F. Wang and K. Lai, "Nanoscale Conductivity Imaging of Correlated Electronic States in WSe2/WS2 Moiré Superlattices," *Physical Review Letters,* vol. 125, p. 186803, 2020.

[8] X. Huang, T. Wang, S. Miao, C. Wang, Z. Li, Z. Lian, T. Taniguchi, K. Watanabe, S. Okamoto, D. Xiao, S.-F. Shi and Y.-T. Cui, "Correlated insulating states at fractional fillings of the WS2/WSe2 moiré lattice," *Nature Physics,* vol. 17, pp. 715-719, 2021.

[9] Y.-T. Cui, B. Wen, E. Y. Ma, G. Diankov, Z. Han, F. Amet, T. Taniguchi, K. Watanabe, D. Goldhaber-Gordon, C. R. Dean and Z.-X. Shen, "Unconventional Correlation between Quantum Hall Transport Quantization," *Physical Review Letters,* vol. 117, p. 186601, 2016.

[10] E. Y. Ma, M. R. Calvo, J. Wang, B. Lian, M. Mühlbauer, C. Brüne, Y.-T. Cui, K. Lai, W. Kundhikanjana, Y. Yang, M. Baenninger, M. König, C. Ames, H. Buhmann, P. Leubner, L. W. Molenkamp, S.-C. Zhang, D. Goldhaber-Gordon, M.

A. Kelly and Z.-X. Shen, "Unexpected edge conduction in mercury telluride quantum wells under broken time-reversal symmetry," *Nature Communications,* vol. 6, p. 7252, 2015.

[11] Y. Shi, J. Kahn, B. Niu, Z. Fei, B. Sun, X. Cai, B. A. Francisco, D. Wu, Z.-X. Shen, X. Xu, D. H. Cobden and Y.-T. Cui, "Imaging quantum spin Hall edges in monolayer WTe2," *Science Advances,* vol. 5, no. 2, p. eaat8799, 2019.

[12] M. Allen, Y. Cui, E. Y. Ma, M. Mogi, M. Kawamura, I. Cosma Fulga, D. Goldhaber-Gordon, Y. Tokura and Z.-X. Shen, "Visualization of an axion insulating state at the transition between 2 chiral quantum anomalous Hall states," *PNAS,* vol. 116, no. 29, pp. 14511-14515, 2018.

[13] Y. Cho, "Scanning Nonlinear Dielectric Microscopy," in *Advances in Imaging and Electron Physics, Vol. 127,* Amsterdam, Elsevier, 2003, pp. 1-57.

[14] W. Kundhikanjana, Y. Yang, Q. Tanga, K. Zhang, K. Lai, Y. Ma, M. A. Kelly, X. X. Li and Z.-X. Shen, "Unexpected surface implanted layer in static random access memory devices observed by microwave impedance microscope," *Semiconductor Science and Technology,* vol. 28, p. 025010, 2013.

[15] S. R. Johnston, Y. Yang, Y.-T. Cui, E. Y. Ma, T. Kämpfe, L. M. Eng, J. Zhou, Y.-F. Chen, M. Lu and Z.-X. Shen, "Measurement of surface acoustic wave resonances in ferroelectric domains by microwave microscopy," *Journal of Applied Physics,* vol. 122, p. 074101, 2017.

[16] Bruker AFM Probes, "The Bruker SCM test sample," 4 December 2012. [Online]. Available: https://www.brukerafmprobes.com/Images/SCMSAMPLE%20App%20Note.pdf. [Accessed 23 June 2022].

[17] B. Zhou, J. Balgley, P. Lampen-Kelley, J.-Q. Yan, D. G. Mandrus and E. A. Henriksen, "Evidence for charge transfer and proximate magnetism in graphene–α–RuCl3 heterostructures," *Physical Review B,* vol. 100, p. 165426, 2019.

[18] D. J. Rizzo, B. S. Jessen, Z. Sun, F. L. Ruta, J. Zhang, J.-Q. Yan, L. Xian, A. S. McLeod, M. E. Berkowitz, K. Watanabe, T. Taniguchi, S. E. Nagler, D. G. Mandrus, A. Rubio, M. M. Fogler, A. J. Millis, J. C. Hone, C. R. Dean and D. N. Basov, "Charge-Transfer Plasmon Polaritons at Graphene/α-RuCl3 Interfaces," *Nano Letters,* vol. 20, no. 12, pp. 8438-8445, 2020.

[19] C. R. Woods, P. Ares, H. Nevison-Andrews, M. J. Holwill, R. Fabregas, F. Guinea, A. K. Geim, K. S. Novoselov, N. R. Walet and L. Fumagalli, "Charge-polarized interfacial superlattices in marginally twisted hexagonal boron nitride," *Nature Communications,* vol. 12, p. 347, 2021.

[20] K. Yasuda, X. Wang, K. Watanabe, T. Taniguchi and P. Jarillo-Herrero, "Stacking-engineered ferroelectricity in bilayer boron nitride," *Science,* vol. 372, no. 6549, pp. 1458-1462, 2021.

[21] Y. Chen, C. Chen, R. Kealhofer, H. Liu, Z. Yuan, L. Jiang, J. Suh, J. Park, C. Ko, H. S. Choe, J. Avila, M. Zhong, Z. Wei, J. Li, Li, S. Li, H. Gao, Y. Liu, J. Analytis, Q. Xia, M. C. Asensio and J. Wu, "Black Arsenic: A Layered Semiconductor with Extreme In-Plane Anisotropy," *Advanced Materials,* vol. 30, p. 1800754, 2018.

[22] H. Wang, M.-L. Chen, M. Zhu, Y. Wang, B. Dong, X. Sun, X. Zhang, S. Cao, X. Li, J. Huang, L. Zhang, W. Liu, D. Sun, Y. Ye, K. Song, J. Wang, Y. Han, T. Yang, H. Guo, C. Qin, L. Xiao, J. Zhang, J. Chen, Z. Han and Z. Zhang, "Gate tunable giant anisotropic resistance in ultra-thin GaTe," *Nature Communications,* vol. 10, p. 2302, 2019.

[23] Y.-C. Lin, H.-P. Komsa, C.-H. Yeh, T. Björkman, Z.-Y. Liang, C.-H. Ho, Y.-S. Huang, P.-W. Chiu, A. V. Krasheninnikov and K. Suenaga, "Single-Layer ReS2: Two-Dimensional Semiconductor with Tunable In-Plane Anisotropy," *ACS Nano,* vol. 9, no. 11, pp. 11249-11257, 2015.

[24] E. Liu, Y. Fu, Y. Wang, Y. Feng, H. Liu, X. Wan, W. Zhou, B. Wang, L. Shao, C.-H. Ho, Y.-S. Huang, Z. Cao, L. Wang, A. Li, J. Zeng, F. Song, X. Wang, Y. Shi, H. Yuan, H. Y. Hwang, Y. Cui, F. Miao and D. Xing, "Integrated digital inverters based on two-dimensional anisotropic ReS2 field-effect transistors," *Nature Communications,* vol. 6, p. 6991, 2015.

[25] X. Wang, K. Yasuda, Y. Zhang, S. Liu, K. Watanabe, T. Taniguchi, J. Hone, L. Fu and P. Jarillo-Herrero, "Interfacial ferroelectricity in rhombohedral-stacked bilayer transition metal dichalcogenides," *Nature Nanotechnology,* vol. 17, pp. 367-371, 2022.

[26] A. Weston, E. G. Castanon, V. Enaldiev, F. Ferreira, S. Bhattacharjee, S. Xu, H. Corte-León, Z. Wu, N. Clark, A. Summerfield, T. Hashimoto, Y. Gao, W. Wang, M. Hamer, H. Read, L. Fumagalli, A. V. Kretinin, S. J. Haigh, O. Kazakova, A. K. Geim, V. I. Fal'ko and R. Gorbachev, "Interfacial ferroelectricity in marginally twisted 2D semiconductors," *Nature Nanotechnology,* vol. 17, pp. 390-395, 2022.

[27] W. Kundhikanjana, Z. Sheng, Y. Yang, K. Lai, E. Y. Ma, Y.-T. Cui, M. A. Kelly, M. Nakamura, M. Kawasaki, Y. Tokura, Q. Tang, K. Zhang, X. Li and Z.-X. Shen, "Direct Imaging of Dynamic Glassy Behavior in a Strained Manganite Film," *Physical Review Letters,* vol. 115, p. 265701, 2015.